

RMS ASYMMETRY: A ROBUST METRIC OF GALAXY SHAPES IN IMAGES WITH VARIED DEPTH AND RESOLUTION.

ELIZAVETA SAZONOV^{1,2}, CAMERON MORGAN^{1,2}, MICHAEL BALOGH^{1,2}, KATHERINE ALATALO^{1,3,4}, JOSE A. BENAVIDES⁵, ASA BLUCK⁶, SARAH BROU⁷, INNOCENZA BUSA⁸, RICARDO DEMARCO^{1,9}, DARKO DONEVSKI^{10,11}, MIGUEL FIGUEIRA^{10,12}, GARRETH MARTIN¹³, VICENTE RODRIGUEZ-GOMEZ¹⁴, JAVIER ROMÁN^{15,16}, AND KATE ROWLANDS^{17,4}

¹Waterloo Centre for Astrophysics, University of Waterloo, Waterloo, ON, N2L 3G1 Canada

²Department of Physics and Astronomy, University of Waterloo, Waterloo, ON N2L 3G1, Canada

³Space Telescope Science Institute, 3700 San Martin Dr, Baltimore, MD 21218, USA

⁴William H. Miller III Department of Physics and Astronomy, Johns Hopkins University, Baltimore, MD 21218, USA

⁵Department of Physics and Astronomy, University of California, Riverside, 900 University Avenue, Riverside, CA 92521, USA

⁶Stocker AstroScience Center, Department of Physics, Florida International University, Miami, FL, 33199, USA

⁷School of Physics, University of New South Wales, NSW 2052, Australia

⁸INAF, Osservatorio Astrofisico di Catania, Via S. Sofia 78, I-95123 Catania, Italy

⁹Institute of Astrophysics, Facultad de Ciencias Exactas, Universidad Andrés Bello, Sede Concepción, Talcahuano, Chile

¹⁰National Centre for Nuclear Research, Pasteura 7, 02-093 Warsaw, Poland

¹¹SISSA, Via Bonomea 265, 34136 Trieste, Italy

¹²Max-Planck-Institut für Radioastronomie, Auf dem Hügel 69, 53121, Bonn, Germany

¹³School of Physics and Astronomy, University of Nottingham, University Park, Nottingham NG7 2RD, UK

¹⁴Instituto de Radioastronomía y Astrofísica, Universidad Nacional Autónoma de México, A.P. 72-3, 58089 Morelia, Mexico

¹⁵Departamento de Astrofísica, Universidad de La Laguna, E-38206, La Laguna, Tenerife, Spain

¹⁶Instituto de Astrofísica de Canarias, c/ Vía Láctea s/n, E-38205, La Laguna, Tenerife, Spain and

¹⁷AURA for ESA, Space Telescope Science Institute, 3700 San Martin Drive, Baltimore, MD, USA

Version April 10, 2024

ABSTRACT

Structural disturbances, such as galaxy mergers or instabilities, are key candidates for driving galaxy evolution, so it is important to detect and quantify galaxies hosting these disturbances spanning a range of masses, environments, and cosmic times. Traditionally, this is done by quantifying the asymmetry of a galaxy as part of the concentration-asymmetry-smoothness system, A_{CAS} , and selecting galaxies above a certain threshold as merger candidates. However, in this work, we show that A_{CAS} , is extremely dependent on imaging properties – both resolution and depth – and thus defining a single A_{CAS} threshold is impossible. We analyze an alternative root-mean-squared asymmetry, A_{RMS} , and show that it is independent of noise down to the average SNR per pixel of 1. However, both metrics depend on the resolution. We argue that asymmetry is, by design, always a scale-dependent measurement, and it is essential to define an asymmetry at a given physical resolution, where the limit should be defined by the size of the smallest features one wishes to detect. We measure asymmetry of a set of $z \approx 0.1$ galaxies observed with *HST*, HSC, and SDSS, and show that after matching the resolution of all images to 200 pc, we are able to obtain consistent $A_{\text{RMS},200\text{ pc}}$ measurements with all three instruments despite the vast differences in the original resolution or depth. We recommend that future studies use $A_{\text{RMS},x\text{ pc}}$ measurement when evaluating asymmetry, where x is defined by the physical size of the features of interest, and is kept consistent across the dataset, especially when the redshift or image properties of galaxies in the dataset vary.

Subject headings: Galaxy structure (622) — Galaxy morphology (582) — astronomy image processing (2306)

1. INTRODUCTION

There is a strong bimodality among galaxies in the local Universe, with two dominant populations: blue star-forming and red quiescent galaxies (e.g., Baldry et al. 2004; Balogh et al. 2004; Taylor et al. 2015). Studies into the origin of this bimodality show that the fraction of star-forming galaxies of a given mass decreases with cosmic time while the fraction of quiescent ones in-

creases, indicating evolution (Bell et al. 2004; Arnouts et al. 2007; Faber et al. 2007). Their stellar structure is also bimodal: while blue galaxies are typically “late-type” disks with prominent spiral arms, most quiescent galaxies are “early-type” with a smooth spheroidal structure (e.g., Strateva et al. 2001; Schawinski et al. 2014), with rare exceptions (e.g., Masters et al. 2010). The existence of a *morphology* bimodality implies that the structure of

galaxies must also evolve during this transition. However, the relative timescales of the two changes, or the causal relationship between star formation and structure are still disputed.

As a result, the processes driving this evolution are also debated, and likely vary from one galaxy to another, depending on many factors such as mass or environment (e.g., Baldry et al. 2006; Peng et al. 2010). A combination of different quenching mechanisms can be responsible for shutting down star formation in a galaxy, temporarily or permanently. Typically, they act in one of three ways: by 1) removing the gas supply, as do supernovae-driven winds (e.g., Heckman et al. 1990; Leroy et al. 2015), winds originating from the active galactic nuclei (e.g., Ciccone et al. 2014), or ram pressure in galaxy clusters (Gunn & Gott 1972; Abadi et al. 1999; Poggianti et al. 2017); 2) triggering a period of rapid star formation that quickly consumes the gas, for example from bar instabilities (e.g., Masters et al. 2012) or radial gas inflows following a merger (e.g., Hopkins et al. 2009); or 3) by preventing the gas from cooling enough to form stars (e.g., through heating by the central black hole or stabilization in the bulge; Benson et al. 2003; Martig et al. 2009; Werner et al. 2019). This list is by far not exhaustive, and many of these mechanisms can (and likely do) act in tandem, or trigger other mechanisms. For example, a galaxy merger may both trigger a starburst and feed the central black hole, leading to rapid gas consumption and its eventual expulsion in massive outflows, while black hole feedback may be needed to ensure star formation does not resume (e.g., Ellison et al. 2013; Piotrowska et al. 2022; Bluck et al. 2023).

Both the gas properties of a galaxy and its structure change as it evolves, however it is still unclear which change occurs first. Therefore, studying the structural impacts of different quenching pathways is crucial. Most physical processes affect the observed morphology in some way: mergers can induce tidal features such as shells or tails (e.g., Toomre & Toomre 1972; Schweizer 1980), outflows can be detected as asymmetric features in gas and dust maps (e.g., Quinn 1984), while bars are identifiable as axisymmetric perturbations (e.g., Ciambur & Graham 2016; Kruk et al. 2018). Detecting disturbances in galaxy imaging can therefore help us identify galaxies which are currently quenching, and provide insight into the ongoing physical mechanisms.

Doing this in a fast, accurate, and an automated way allows studying large sets of galaxies, and quickly leveraging large surveys, such as Sloan Digital Sky Survey (SDSS; York et al. 2000; Blanton et al. 2017). Upcoming surveys, such as Rubin Observatory’s Legacy Survey of Space and Time (LSST; Ivezić et al. 2019) and the Euclid survey (Collaboration et al. 2022a), will provide an unprecedented dataset of billions of galaxies, includ-

ing low surface brightness ones that were challenging to study before. Thus, a set of structural measurements are needed to detect and quantify structural disturbances for these large datasets.

A classic one is the measurement of a galaxy’s asymmetry (e.g., Schade et al. 1995; Abraham et al. 1996). Currently, the most widely used metric is the asymmetry defined as part of the concentration-asymmetry-smoothness parameter system (CAS; Conselice et al. 2000; Conselice 2003), hereafter A_{CAS} , calculated by rotating the image by 180°, finding the absolute residual between the original and the rotated images, and computing the ratio of this residual to the total flux. This metric is sensitive to bright regions that deviate from an otherwise symmetric profile, and has traditionally been used to detect major mergers (e.g., Conselice et al. 2008; Lotz et al. 2011). Recently, A_{CAS} has been shown to detect a broader set of features: disrupted dust structure (e.g., Sazonova et al. 2021), clumpy star formation (e.g., Ferreira et al. 2022), outflows in HI maps (Deg et al. 2023; Holwerda et al. 2011), and more.

However, the A_{CAS} measurement is highly dependent on both image resolution and signal-to-noise ratio (e.g., Lotz et al. 2004; Giese et al. 2016; Bottrell et al. 2019; Bignone et al. 2020; Thorp et al. 2021). Therefore, comparing measurements of asymmetry across datasets is challenging. A_{CAS} measured on noisy or poorly resolved images can miss important features, so using this metric alone can lead to underestimating the fractions of merging or disturbed galaxies (e.g., Snyder et al. 2019; Sazonova et al. 2021; Wilkinson et al. 2024). Newer approaches have been developed that address some of these issues: for example, shape asymmetry, which is insensitive to image resolution (Pawlik et al. 2016); neural networks (e.g., Domínguez Sánchez et al. 2018; Walmsley et al. 2022; Desmons et al. 2023), or visual classification schemes (e.g., Galaxy Zoo; Lintott et al. 2008; Willett et al. 2013).

Despite its strong dependence on image quality, the traditional A_{CAS} measurement is advantageous in that it is easy to interpret (unlike many machine learning methods) and is relatively fast to compute on large datasets. Moreover, A_{CAS} is widely used to this day and thus enables easy comparisons between studies, provided similar imaging quality or source redshifts. To make A_{CAS} more robust, various methods to correct for the impact of noise or resolution on A_{CAS} have been proposed (Shi et al. 2009; Wen & Zheng 2016; Thorp et al. 2021; Yu et al. 2023). However, while the numerical performance of A_{CAS} has been tested, few studies have tested the mathematical definition of A_{CAS} and its *expected* behavior to varying noise or resolution. Thorp et al. (2021) show that the background contribution is always overestimated in the A_{CAS} measurement and provide a correc-

tion, while [Conselice et al. \(2000\)](#) qualitatively note that asymmetry depends on resolution.

In this paper, we mathematically show that A_{CAS} depends strongly on background due to the absolute-valued definition, while the resolution dependence arises from both the pixelation and the smearing by the point spread function (PSF). Similarly to [Deg et al. \(2023\)](#), we propose to instead use the root-mean-square asymmetry, A_{RMS} , as initially considered in [Conselice \(1997\)](#) and [Conselice et al. \(2000\)](#).

We then perform a series of simulations using GALSIM ([Rowe et al. 2015](#)) and test the dependence of both A_{CAS} and A_{RMS} on image noise and resolution. We further test these measurements on a pilot dataset of 27 galaxies studied in [Sazonova et al. \(2021\)](#), which span a range of morphologies and degrees of disturbance, and are observed with the the Hubble Space Telescope (*HST*), SDSS, and Hyper-Suprime Cam (HSC; [Aihara et al. 2022](#)), thereby sampling different image depths and resolution. Finally, we use our results to provide guidelines on which parameter performs best in different experimental set-ups.

The paper is organized as follows. We describe the GALSIM simulations used throughout the paper in Section 2. In Section 3, we show the original A_{CAS} definition and demonstrate its mathematical dependence on noise and the PSF size. We also propose a slight modification that alleviates some of the noise dependence. In Section 4, we introduce the A_{RMS} measurement and show that it has no dependence on noise, but a higher dependence on resolution. We test the performance of these metrics on real data from the SDSS, *HST*, and HSC data for the same set of galaxies in Section 5. Finally, we discuss our findings and provide guidelines for the use of the different asymmetry parameters in Section 6.

Throughout this work, we use the Planck 2018 cosmology ($H_0=67.6$, $\Omega_m=0.310$; [Collaboration et al. 2020](#)) to convert between angular and physical sizes.

2. GALSIM MOCK IMAGES

To test the performance of the asymmetry metrics, we need to compare the asymmetry measured using an imperfect “observed” image to the “true” asymmetry of a galaxy. Since the “true” asymmetry of real galaxies is unknown, we use a simulated dataset, and then test our results on a sample of observed galaxies (Section 5). However, even for simulated objects, estimating a “true” asymmetry is impossible: since any numerical calculation requires evaluating asymmetry on some discretized pixel grid, any calculation will depend on the chosen resolution. Instead, we simulate pairs of galaxies: a “baseline” image, which represents the best-case scenario least affected by observational biases, and an “observed” or “mock” image with varying resolution and depth.

TABLE 1
GALSIM PARAMETER DISTRIBUTIONS

Parameter	Distribution
Galaxy properties	
$r\text{-mag}$	Uniform (11, 18)
Sérsic n	Uniform (1, 5)
R_{eff} [arcsec]	$-1.9 \times r\text{-mag} + 35 + \mathcal{N}(0, 1.5)$
Orientation	Uniform (0, 2π)
Ellipticity	0 if $n > 3.5$ else Uniform (0,1)
Clump properties	
N	Discrete Uniform (5, 30)
Flux fraction	Log-Uniform (10^{-3} , 0.5)
Size [arcsec]	Uniform (0.1, 3)
θ	Uniform (0, 2π)
r/R_p	Uniform (0.05, 1)
Mock image properties	
Pixel scale [arcsec]	Uniform (0.1, 0.5)
PSF FWHM [arcsec]	Uniform ($2 \times$ pixel scale, 3)
Sky σ [mag/arcsec 2]	Uniform (20, 26)

While we could have used realistic galaxies from cosmological simulations such as Illustris TNG ([Pillepich et al. 2018](#); [Nelson et al. 2019](#); [Rodriguez-Gomez et al. 2019](#); [Bottrell et al. 2024](#)) or higher-resolution zoom-in simulations (e.g., [Ceverino et al. 2014](#); [Hopkins et al. 2018](#)), all numerical simulations still have a limited spatial resolution and do not reproduce clumps smaller than the softening scale. Moreover, while they provide large datasets in general, there is a limit to how many highly asymmetric galaxies we can obtain from simulations since merging galaxies are rare. Instead, we opted for a simpler approach: we produced mock observations using GALSIM ([Rowe et al. 2015](#)), which produces an image given a set of user-input light distributions and perturbation parameters. This also gave us freedom in varying both the depth and resolution of simulated images. Our approach to use a single Sérsic profile with Gaussian clumps is essentially the same as that taken to create the Rubin Data Preview 0 dataset ([LSST Dark Energy Science Collaboration et al. 2020](#)).

We defined each galaxy as a single two-dimensional Sérsic profile ([Sérsic 1963](#)) with a variable total flux, Sérsic index n , orientation, half-light radius R_{eff} , and ellipticity. We used the PETROFIT package ([Geda et al. 2022](#)) to calculate the Petrosian radius (R_p , [Petrosian 1976](#)), based on the Sérsic index and half-light radius for future steps. PETROFIT calculates the ratio of the mean global brightness to the isophotal brightness as a function of radius for a given n and R_{eff} , and we picked the radius where this value is equal to 0.2 as R_p . For each object, the magnitude, n , R_{eff} , orientation, and ellipticity were randomly drawn from the distributions in Table 1. The range of values was chosen to produce galaxies consistent with observed $z \approx 0.1$ objects used in Section 5. The R_{eff}

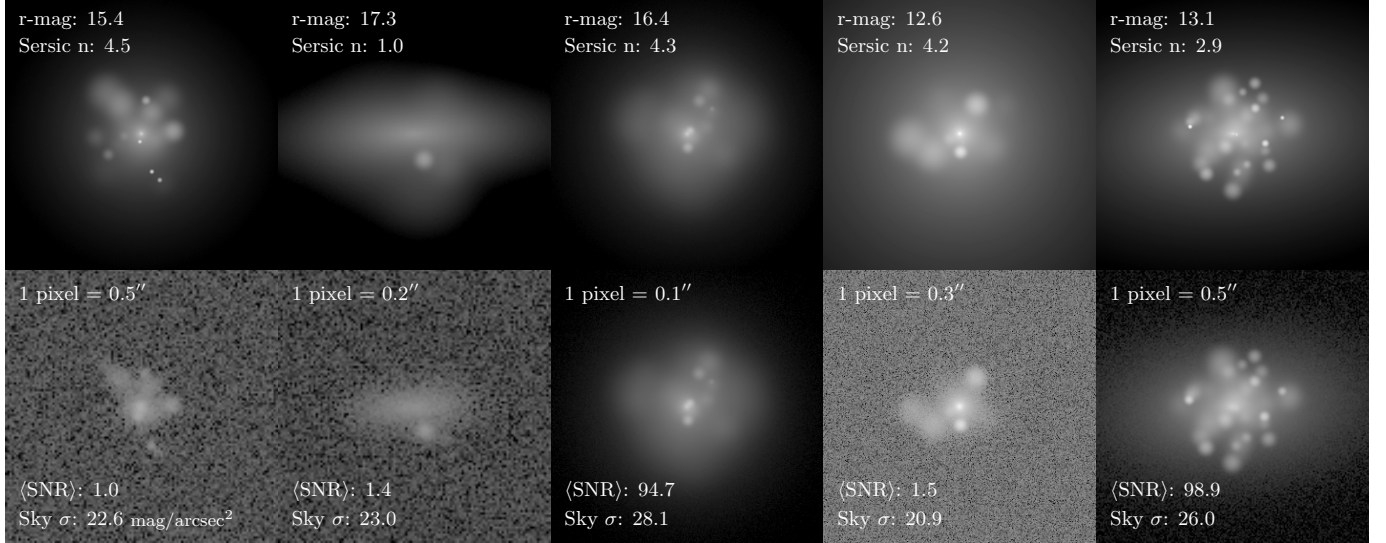


FIG. 1.— A random sample of baseline simulated galaxies (**top**) and their mock observations (**bottom**). Each galaxy is generated as a combination of a Sérsic profile and a set of Gaussian clumps using a set of parameters randomly drawn from a distribution summarized in Table 1. The mock image is then generated with a different pixel scale, convolved with a Gaussian PSF, then has a sky background and Poisson noise applied. The pixel scale and 1σ image depth are also randomly drawn and shown here for each mock image. The PSF FWHM is chosen to be 3 times the pixel scale to ensure Nyquist sampling. The $\langle \text{SNR} \rangle$ is calculated within a $1.5R_p$ aperture around the source.

distribution is derived from estimating the relationship between R_{eff} and r -magnitude and its scatter in SDSS galaxies.

To create asymmetric features in our simulated galaxies, we added N Gaussian clumps on top of the Sérsic profile. Each clump is defined using its own size (Gaussian σ), a flux fraction relative to the total flux of the Sérsic component, and a location given by an angle θ and a radius from the galaxy’s center, r/R_p . All model parameters are again drawn from distributions summarized in Table 1.

Our Gaussian clumps mimic various disturbances seen in real galaxies: small clumps embedded in the disk are most similar to star-forming clumps; off-axis small clumps can be viewed as satellite galaxies, while large and far-removed faint clumps are similar to tidal features. This is clearly an over-simplification of the structure of real galaxies, and does not produce true merger-like structures such as tidal tails. However, the aim of this work is not to devise a metric that is sensitive to a particular disturbance, but to test the performance of existing metrics with regards to the image quality, and these simplistic distributions allow us to test this efficiently. We note that both A_{CAS} and A_{RMS} calculate the total flux in the residual after a rotation (see Sections 3 and 4). Therefore, the values depend on the size and the brightness of disturbed features, but not on their shape or distance from the galactic disk, so the numerical performance on more realistic distributions will remain the same. Since our tests span a wide range of sizes and relative fluxes, we can investigate the performance of the metrics despite our simple galaxy models.

At this stage, the idealized galaxy is described purely by a set of analytical functions and does not suffer from any observational effects. We then construct the “baseline” image. We create a blank patch of sky with a field-of-view of $10R_p$ and a pixel scale of $0.1''$. Note that at this stage, we must assume a resolution limit – we opted for a pixel scale of $0.1''$ per pixel (~ 200 pc at $z=0.1$), comparable to that of space-based imaging (e.g., Euclid), as higher-resolution simulations become computationally intensive even with the GALSIM approach. Since the image should be Nyquist-sampled, we convolve the model with a Gaussian PSF whose full width at half maximum (FWHM) is three times the size of the pixel scale, similar to typical telescope designs (e.g. SDSS, HSC)¹. Thus, the effective resolution of our baseline images is $0.3''$. We then add the galaxy model to the sky patch assuming an SDSS r -band bandpass and transmission curve.

After this, we add a low-level uniform sky background that, based on Poisson statistics, would produce sky noise surface brightness (SB) of 30 mag/arcsec^2 in a blank region of the image. The SB is calculated using the pixel-by-pixel 1σ standard deviation of the sky. Note that this is a different depth definition than that used in survey design, where either an $N\sigma$ point-source depth or depth within a detection area are often quoted (e.g., Ivezić et al. 2019; Román et al. 2020). When the goal is source detection, these depth metrics are preferable. However, since we are interested in pixel-by-pixel flux variations, we opt for using a pixel-by-pixel surface brightness metric in

¹ Note that while Nyquist sampling requires at least 2 resolution elements per PSF FWHM, since pixels are two-dimensional, the requirement along the diagonal becomes $2\sqrt{2} \approx 2.8$ pixels, hence we choose a PSF FWHM that spans 3 pixels

stead since it more directly relates to the features we aim to measure.

Finally, we convert the image to electron counts, apply Poisson noise to the whole image, and subtract the mean sky level to get our baseline image. To create a mock observation, we repeat the same steps with a different resolution and noise level, both drawn from the respective distributions in Table 1. While we do not set the $\langle \text{SNR} \rangle$ manually, we calculate it by taking the mean SNR within the aperture in which asymmetry is calculated. We run three series of tests, as described in detail in Section 3: with varying sky surface brightness, varying pixel scale, and varying aperture size. For each series of tests, we generated 1,000 GALSIM galaxies. Examples of some baseline and mock observations are shown in Fig. 1 (top and bottom rows respectively).

Our simulations and mock observations are tuned to roughly match the imaging of relatively local ($z \sim 0.1$) galaxies of different masses; however, the important factors we study are the impact of the spatial resolution and depth. The implications of our results can be easily applied to observations of higher-redshift objects, since higher-redshift objects observed within the same survey have a lower physical resolution and SNR.

3. CAS ASYMMETRY

The most common way to measure asymmetry is to find the absolute difference in flux distributions under a 180° rotation, first defined in Schade et al. (1995) and Abraham et al. (1996). The current implementation of this metric is A_{CAS} , described in Conselice et al. (2000) and Conselice (2003). It is calculated in the following way.

An image consists of some light distribution, $I(x, y)$, which is discretized at each pixel as I_{ij} . The image is rotated by 180 degrees about the center \mathbf{x}_0 to get the flux of the rotated image, I_{ij}^{180} . Then asymmetry is calculated in as:

$$A_{\text{CAS}} = \min_{\mathbf{x}_0} \frac{\sum_{ij} |I_{ij} - I_{ij}^{180}|}{\sum_{ij} |I_{ij}|} - \langle A_{\text{CAS},bg} \rangle \quad (1)$$

where $\langle A_{\text{CAS},bg} \rangle$ is the average background asymmetry, which we describe in detail below. The sum is performed in an aperture of size fR_p centered on \mathbf{x}_0 . The value of f typically ranges between 1 and 2 with most codes adopting $f = 1.5$ by default (e.g., the `statmorph` code; Rodriguez-Gomez et al. 2019), although larger f may be needed for very bulge-dominated galaxies as galaxy flux extends significantly past $2R_p$ (Graham & Driver 2005). In some cases, where the underlying distribution is too clumpy to compute R_p , instead an aperture derived from another band may be used (e.g., Holwerda et al. 2012, 2023). Finally, while most often the aperture is circular, elliptical apertures can be adopted for highly inclined

galaxies to minimize the impact of the sky background (e.g., MORFOMETRYKA; Ferrari et al. 2015).

The crucial steps of this calculation are 1) calculating the background contribution $A_{\text{CAS},bg}$ and 2) choosing the coordinate \mathbf{x}_0 that minimizes the asymmetry. Both of these steps include several caveats and can be implemented in different ways. The choices for the minimization algorithm can affect the measurement, as we show in Appendix A. However, correctly treating the background is even more challenging.

The sky may have large-scale asymmetries (e.g., gradients), which need to be subtracted from the image to not affect the measurement. However, even if the large-scale background is perfectly subtracted, the Poisson noise from the sky counts will still affect the calculation as it contributes to the absolute value of the residuals. Therefore, the contribution from the background *noise* needs to be corrected for. Calculating the background asymmetry in the same aperture as the source is impossible, and most codes approximate it from a blank patch of sky in some way, which we discuss in detail in Appendix B. However, it is worth noting here that a common approach is to calculate the asymmetry in a blank sky aperture (we use a circular annulus around the source), and then re-normalize the background noise contribution by the ratio of the sizes of the sky and the source apertures (N_{sky} and N_{ap} respectively). Assuming the image is background-subtracted, the correction is

$$\langle A_{\text{CAS},bg} \rangle = \frac{N_{\text{ap}}}{N_{\text{sky}}} \frac{\sum_{ij}^{\text{sky}} |\epsilon_{ij} - \epsilon_{ij}^{180}|}{\sum_{ij} |I_{ij}|} \quad (2)$$

where $\epsilon(x, y)$ is the sky flux distribution and ϵ_{ij} is its discretized version. In the case of a flat and a subtracted sky background the noise is normally-distributed, i.e. $\langle \epsilon \rangle = 0$. We note that since the background correction is absolute-valued it is always positive, so it will always decrease the measured asymmetry.

Without any background contribution, A_{CAS} would theoretically vary between 0 and 2. However, since \mathbf{x}_0 minimizes asymmetry, $A_{\text{CAS}} = 2$ is unlikely, and in most cases $0 < A_{\text{CAS}} \lesssim 1$. Typically, a threshold $A_{\text{CAS}} > 0.3$ is used to select mergers, although as we show in this work this threshold should depend on the imaging properties. Since $\langle A_{\text{CAS},bg} \rangle$ is always positive, then if the image is noisy and the galaxy is undisturbed, the resultant A_{CAS} can be slightly negative (e.g., as shown in Rodriguez-Gomez et al. 2019).

3.1. Numerical performance

We investigated the numerical performance of A_{CAS} using a series of tests, the results of which are shown in Fig. 2. For each series, we generated 1,000 galaxies with random physical properties as described in Sec. 2 (except the third series, discussed below), and compared

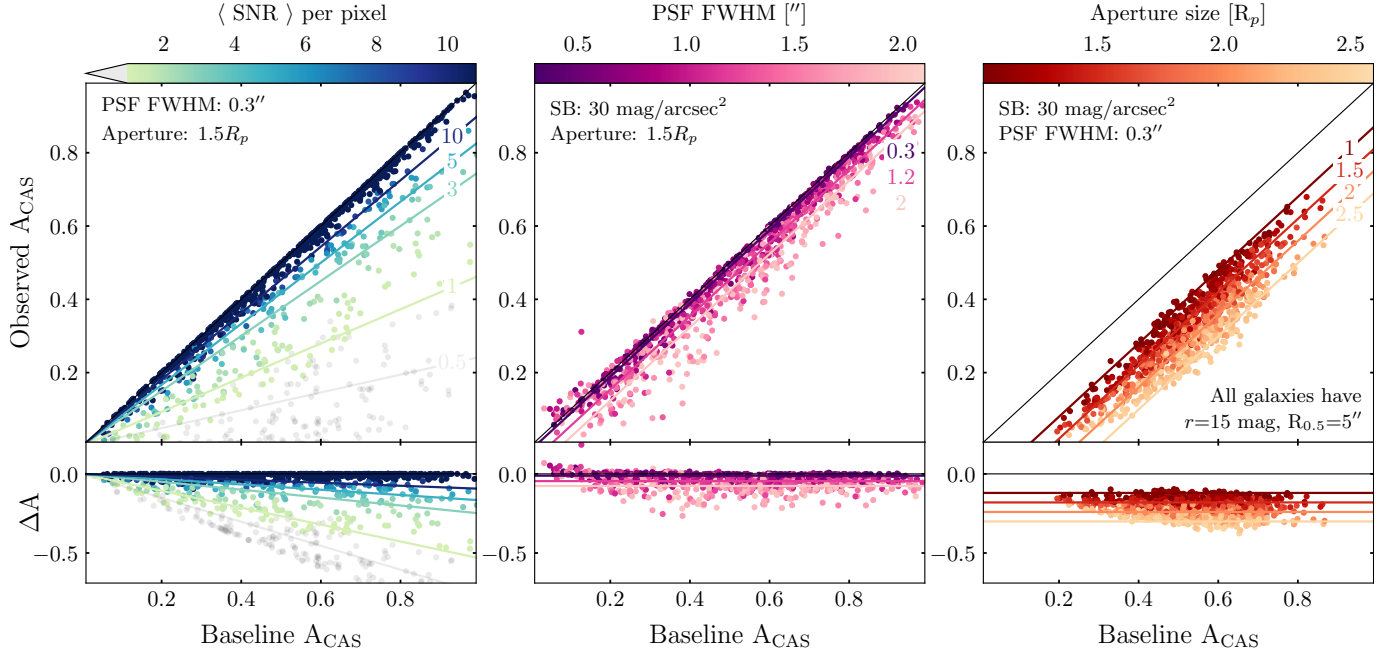


FIG. 2.— The comparison (**top**) and the difference (**bottom**) of A_{CAS} measured using mock observations (y-axis) and a baseline image (x-axis) for three series of tests on simulated galaxies: varied $\langle \text{SNR} \rangle$ while resolution is fixed to the baseline resolution (**left**), varied resolution with a fixed baseline depth (**center**), and varied aperture size with a fixed resolution, depth, and galaxy size and flux (**right**). The diagonal line shows a 1-to-1 relationship between the measured and baseline asymmetries. Solid lines represent best fits to the dependence of observed A_{CAS} on the baseline A_{CAS} and $\langle \text{SNR} \rangle$, PSF size, and aperture size as described in Sec. 3. A_{CAS} is only weakly dependent on resolution in these tests, but it is significantly underestimated in shallow images compared to the deep baseline ones. This effect depends on the intrinsic asymmetry of the object, where A_{CAS} of disturbed galaxies is *more* underestimated. Finally, even for a fixed image quality, A_{CAS} depends on the aperture size, i.e. the number of blank background pixels included in the measurement.

the asymmetry calculated using the baseline ($\text{SB}=30 \text{ mag/arcsec}^2$, $0.1''$ pixel scale) and the observed images, shown on the x- and y-axis respectively. We first looked at how observed A_{CAS} changes with image depth (left panel), then with the resolution (middle panel), and finally with aperture size (right panel). For the aperture size tests, we generated all galaxies with $r=15 \text{ mag}$ and $R_{\text{eff}}=5''$, to keep the total flux, and hence the total SNR, roughly constant and ensure only the aperture changes affect the result. In all panels, the solid diagonal line shows a 1-to-1 relationship, or ideal performance compared to the baseline image.

For each series of tests, we fit the relationship between the observed and the baseline A_{CAS} using two models: an exponential and a linear offset, shown below.

$$[\text{Model 1}] \quad A_{\text{CASobs}} = A_{\text{CASbase}} \exp \left[- \left(\frac{p}{\tau_p} \right)^{\alpha_p} \right]$$

$$[\text{Model 2}] \quad A_{\text{CASobs}} = A_{\text{CASbase}} - m_p \times p$$

where p is some variable ($\langle \text{SNR} \rangle$, PSF FWHM, or aperture size), and τ , α , and m are parameters to be fit for each variable. We adopt the fit with the lowest root-mean-squared error divided by the degrees of freedom. We discuss the trends seen in each panel below, and then show how the mathematical formula for A_{CAS} gives rise to these trends in Sec. 3.2.

Signal-to-noise ratio. The left panel shows how the

observed A_{CAS} changes with $\langle \text{SNR} \rangle$, while the resolution is fixed to $0.1''$, same as the baseline image. The color gradient indicates decreasing $\langle \text{SNR} \rangle$ from > 10 (dark blue) to 1 (light green). Points with $\langle \text{SNR} \rangle < 1$ are colored in grey.

The best-fitting model is the exponential decay:

$$A_{\text{CASobs}} = A_{\text{CASbase}} \exp \left[- \left(\frac{\langle \text{SNR} \rangle}{0.74} \right)^{-0.89} \right] \quad (3)$$

so that the observed A_{CAS} approaches 0 as $\langle \text{SNR} \rangle$ decreases, and approaches the baseline value as $\langle \text{SNR} \rangle$ grows to infinity. We show the resulting lines of best fit for five different $\langle \text{SNR} \rangle$ levels in Fig. 2. Our results are qualitatively consistent with previous results (e.g., Bottrell et al. 2019; Thorp et al. 2021): measured A_{CAS} decreases with $\langle \text{SNR} \rangle$. However, our exponential model is more realistic than a polynomial fit derived in Thorp et al. (2021) as it provides more physically motivated constraints to the measured asymmetry, ensuring that it is bound between 0 and the baseline value.

Most crucial is the fact that the bias between the measured and baseline A_{CAS} depends not only on $\langle \text{SNR} \rangle$ but also on the intrinsic asymmetry: galaxies with higher intrinsic A_{CAS} suffer a larger measurement bias. Therefore, the dynamic range of A_{CAS} in shallow imaging is low, making it more difficult to distinguish between disturbed and regular galaxies. For example, for SDSS-like imaging

($\langle \text{SNR} \rangle \sim 1$) a measured $A_{\text{CAS}} = 0.2$ maps to a wide range of intrinsic asymmetries between $0.2 < A_{\text{CAS, true}} < 0.8$, making it impossible to distinguish irregular and normal galaxies. Therefore, it is important to recognize that both the A_{CAS} threshold to select disturbed objects must change for different datasets, and that we may only be able to detect extremely asymmetric galaxies in shallow imaging. While a correction can be applied, the scatter is also larger at lower $\langle \text{SNR} \rangle$ values, making the correction less reliable in noisy images.

Resolution. The middle panel in Fig. 2 shows the dependence of A_{CAS} on resolution, or PSF FWHM, in mock images with a fixed sky surface brightness (SB) of 30 mag/arcsec². Measured asymmetry decreases with resolution, as was previously found in other studies (Lotz et al. 2004; Giese et al. 2016; Bignone et al. 2020; Thorp et al. 2021), although the dependence is weaker than the dependence on $\langle \text{SNR} \rangle$. The best fit to our data is a small linear offset:

$$A_{\text{CAS, obs}} = A_{\text{CAS, base}} - 0.038 \times \text{PSF FWHM} \quad (4)$$

Interestingly, Thorp et al. (2021) report that the resolution-dependent error in A_{CAS} is stronger and also depends on the *intrinsic* asymmetry of the object, but we do not find this bias. This difference may be due to a difference in our simulated data. While Thorp et al. (2021) use realistic galaxies drawn from Illustris TNG, we use simplistic Sérsic+Gaussian models described in Sec. 2. In our set of simulations, since the size and brightness of clumps are drawn from a random distribution, a galaxy is equally likely to have large-scale and small-scale disturbances. In other words, it is possible to have a galaxy with high intrinsic A_{CAS} with only large clumps, or only small ones, or some fraction of both. Moreover, our clumps are circular, so we do not have asymmetric features that are large along one axis and small (or unresolved) along another, such as spiral arms. On the other hand, this is not true for realistic galaxies. First, real galaxies have spiral arms, that may contribute to asymmetry if perturbed. Galaxies with high intrinsic asymmetry may also have preferentially more small-scale features than symmetric galaxies, due to the physical difference between the two populations. For example, passively evolving galaxies will have a low A_{CAS} and no small-scale star-forming clumps, while star-forming galaxies will typically have larger A_{CAS} and more clumps, and large-scale features (spiral arms) that correlate with small-scale ones (star-forming regions). Mergers lead to both large A_{CAS} and can induce star formation (e.g., Ellison et al. 2008). Thus if the relative number of small, unresolved features correlates with the overall A_{CAS} , then measured asymmetry will depend both on the resolution and intrinsic asymmetry. However, this is due to this secondary cor-

relation rather than the numerical performance of the metric.

Dependence on aperture size. Finally, the rightmost panel in Fig. 2 shows the measured A_{CAS} for a series of tests where galaxies were generated with a similar total SNR, a fixed sky background level of 23 mag/arcsec², and a resolution of 0.1''. We randomly drew an aperture size, ranging between $1R_p$ and $2.5R_p$, and calculated both the baseline and observed A_{CAS} in that aperture to see how the size affects the measurement. Increasing the aperture leads to a larger underestimate of the baseline A_{CAS} . The best fit to the aperture dependence is a linear offset:

$$A_{\text{CAS, obs}} = A_{\text{CAS, base}} - 0.12 \times fR_p \quad (5)$$

Note that the aperture dependence incorporates two effects: the dependence of the measurement on the *total* SNR (i.e., total flux of the galaxy), and on $\langle \text{SNR} \rangle$. Since all galaxies generated in this test have similar total fluxes and hence total SNR, the difference seen here is entirely due to changing the effective $\langle \text{SNR} \rangle$ as the aperture size increases and includes more background flux. However, even for small apertures, there is still an offset from the diagonal due to the low total SNR, the effect seen in the left panel of Fig. 2. While we provide the fit to the linear offset here, the real correction must be applied by recalculating the $\langle \text{SNR} \rangle$ for each object using Eq. 3.

Ideally, if the background correction performs as expected, then adding more background pixels should not affect the final asymmetry, since their contribution is subtracted. However, as is clear in the panel, the bias depends linearly on the aperture size, with larger apertures being further away from the baseline measurement. This is important to keep in mind, since aperture size will depend both on the code implementation and the way R_p is estimated.

3.2. The problem is absolute

The reasons for the noise and resolution dependence of A_{CAS} stem from its mathematical definition, as previously mentioned in Thorp et al. (2021). Here we expand on this discussion by considering the *true* intrinsic CAS asymmetry of a galaxy, before an observation is taken – the ideal noiseless measurement we would like to recover. A galaxy can be described by some surface brightness distribution, $\mathcal{I}(x, y)$, so its true asymmetry is:

$$A_{\text{CAS, true}} = \min_{\mathbf{x}_0} \frac{\int_{\mathbb{R}^2} |\mathcal{I} - \mathcal{I}^{180}| d\mathbf{x}}{\int_{\mathbb{R}^2} |\mathcal{I}| d\mathbf{x}}. \quad (6)$$

In reality, all astronomical observations are discretized to some pixel scale, so we also discretize the intrinsic light distribution. Note that at this stage, subpixel information is lost, so this is no longer strictly a “true”

asymmetry as it will underestimate the effect of small-scale disturbances. The discretized noiseless asymmetry is:

$$A_{\text{CASnoiseless}} = \min_{\mathbf{x}_0} \frac{\sum_{ij} |\mathcal{I}_{ij} - \mathcal{I}_{ij}^{180}|}{\sum_{ij} |\mathcal{I}_{ij}|}. \quad (7)$$

In an observation, the light from the galaxy is overlayed on some back- and foreground flux $I_{\text{sky}}(x, y)$, which may include the Earth's sky, stars, other galaxies, or other sources. It is then blurred, or convolved, with a PSF $\lambda(x, y)$, discretized on the chip, and is subject to a Poisson noise, ϵ . Therefore, the *observed* intensity is:

$$I_{ij} = \left(\lambda * (\mathcal{I}(x, y) + I_{\text{sky}}(x, y)) \right)_{ij} + \epsilon_{ij} \quad (8)$$

if there are sufficiently many electron counts and the Poisson noise can be approximated as Gaussian, ϵ_{ij} is normally distributed with $\epsilon_{ij} \sim \mathcal{N}(0, I_{ij}^2) \sim \mathcal{N}(0, ((\lambda * \mathcal{I})_{ij} + (\lambda * I_{\text{sky}})_{ij})^2)$.

In general, this is a difficult function to deal with. However, we can show that the noise and resolution dependencies arise even with the simplest possible assumptions.

3.2.1. Noise dependence

In the best case scenario, we can assume that the background is flat and subtracted, and ignore the contribution from the source Poisson noise², so that the noise is effectively a Gaussian centered at 0 with a variance σ_{sky}^2 . In this section, we also ignore the effects of the PSF by setting $\lambda = 1$. We can then write the observed distribution simply as:

$$I_{ij} = \mathcal{I}_{ij} + \epsilon_{ij} \quad (9)$$

where $\epsilon_{ij} \sim \mathcal{N}(0, \sigma_{\text{sky}}^2)$.

We can now substitute this flux distribution in Eq. 1 to calculate A_{CAS} . Ignoring the minimization step, we get:

$$A_{\text{CAS}} = \frac{\sum_{ij} |(\mathcal{I}_{ij} - \mathcal{I}_{ij}^{180}) + (\epsilon_{ij} - \epsilon_{ij}^{180})|}{\sum_{ij} |\mathcal{I}_{ij} + \epsilon_{ij}|} - \langle A_{\text{CAS},bg} \rangle. \quad (10)$$

Using the typical implementation of the $\langle A_{\text{CAS},bg} \rangle$ term (Eq. 2), and omitting the aperture normalization term $N_{\text{ap}}/N_{\text{sky}}$ for clarity, the calculation is then:

² In real observations, noise originates both from the sky and the source itself. Although we do not model the Poisson noise from the source here, we note that in simulated galaxies used in our tests, both the baseline and the mock image have a Poisson noise contribution, but the Poisson noise does not significantly affect our results. This may be different for observations with low photon counts, such as ultraviolet or X-ray ones.

$$A_{\text{CAS}} = \frac{\sum_{ij} |(\mathcal{I}_{ij} - \mathcal{I}_{ij}^{180}) + (\epsilon_{ij} - \epsilon_{ij}^{180})| - \sum_{ij} |\epsilon_{ij} - \epsilon_{ij}^{180}|}{\sum_{ij} |\mathcal{I}_{ij} + \epsilon_{ij}|}. \quad (11)$$

An ideal measurement should recover the noiseless asymmetry in Eq. 7. However, the use of an absolute-valued function means that the equation above does not reduce to Eq. 7, even with our simplified assumptions. As pointed out in Thorp et al. (2021), using the triangle inequality $(|a + b| - |b| \leq A_{\text{CAS}})$ it is apparent the numerator underestimates the true asymmetry. Moreover, the denominator (typically) is not corrected for the noise contribution at all.

Assuming that the galaxy is much brighter than the sky (i.e. in the high $\langle \text{SNR} \rangle$ regime), the denominator can be approximated as $|\mathcal{I}_{ij} + \epsilon_{ij}| \approx |\mathcal{I}_{ij}| + |\epsilon_{ij}|$ and it may be possible to subtract the noise term. However, in the numerator, both the source residual $\mathcal{I} - \mathcal{I}^{180}$ and the noise residual $\epsilon_{ij} - \epsilon_{ij}^{180}$ may vary in signs while having similar magnitudes. If the underlying galaxy is bright but symmetric, it is possible to have $|\mathcal{I} - \mathcal{I}^{180}| \approx |\epsilon_{ij} - \epsilon_{ij}^{180}|$, making the sum inseparable. Therefore, even in the high-SNR regime, the calculation will not recover the true asymmetry in some cases.

In practice, this leads to a complex behaviour. In the low- $\langle \text{SNR} \rangle$ regime, the noise contributes to both the numerator and the denominator, leading to over-subtraction of the noise with the $A_{\text{CAS},bg}$ term in the numerator, and the over-normalization in the denominator. This means that A_{CAS} will produce a biased measurement, as seen in the left panel of Fig. 2, for low- $\langle \text{SNR} \rangle$ galaxies. In the high- $\langle \text{SNR} \rangle$ regime, the denominator approximates $\sum \mathcal{I}_{ij}$ and does not add a significant measurement error, while the measurement error in the numerator scales with the intrinsic asymmetry. In either case, the noise dependence of the A_{CAS} measurement cannot be easily subtracted and correlates with the intrinsic asymmetry of the source.

3.2.2. Dependence on the aperture

An important consequence of the $\langle \text{SNR} \rangle$ dependence is the dependence of A_{CAS} on the aperture in which it is calculated. Since the denominator in Eq. 1 is not corrected for the background noise, adding blank sky pixels increases the denominator. Therefore, A_{CAS} measurement decreases with aperture size. We show this for one of the simulated galaxies in Fig. 3. A_{CAS} measured on the baseline and the observed images are shown in black and yellow, respectively. The purple line corresponds to the corrected A_{CAS} , which we discuss below in Sec. 3.2.3.

For apertures smaller than the galaxy (grey-shaded region in Fig. 3), all A_{CAS} measurements increase with the aperture size as we include more asymmetric features.

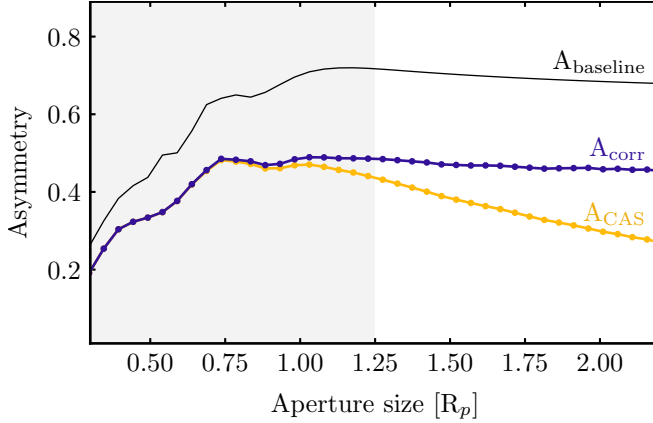


FIG. 3.— The dependence of A_{CAS} measurements on aperture size for one simulated galaxy ($n=3.3$, $r\text{-mag}=14$) with sky surface brightness of 22 mag/arcsec^2 , showing the baseline A_{CAS} (black), observed A_{CAS} (yellow), and a corrected measurement A_{CAScorr} (as defined in Sec. 3.2.3, purple). All asymmetric clumps in the GALSim run are placed within $1R_p$, so the baseline asymmetry flattens out at $\sim 1.2R_p$ (unshaded region). Beyond this radius, only the background noise contributes to the baseline A_{CAS} measurement. A_{CAScorr} also flattens out, indicating a better noise correction, while the observed A_{CAS} continues to decrease as more sky pixels are included in the aperture. However, both A_{CAS} and A_{CAScorr} underestimate the baseline A_{CAS} .

However, once the aperture exceeds the extent of the galaxy and includes additional sky pixels, the measurements should flatten out and converge on a single value. We see this for $A_{\text{CASbaseline}}$, but not for the observed A_{CAS} . As more sky is included in the aperture, its contribution to the absolute flux increases. The residual term in the numerator corrects for this (albeit not fully), while the normalization term in the denominator of A_{CAS} does not. Therefore, the denominator term increases as the aperture grows, leading to lower A_{CAS} values.

The aperture dependence is important to consider. Different software packages use different aperture sizes in which asymmetry is calculated (e.g., $1.5R_p$ in Rodriguez-Gomez et al. (2019) and the maximum radius in the A_{CAS} calculation in Pawlik et al. (2016)). Moreover, finding R_p in itself is non-trivial, and so different packages may produce different radii, even if the fraction of R_p is kept the same. As a result, catalogs produced with different algorithms will give systematically offset A_{CAS} measurements on the same images.

3.2.3. A noise correction

The noise dependence of A_{CAS} has been noted since the parameter's introduction in Conselice et al. (2000), and several solutions have been proposed. Giese et al. (2016) suggested using a library of simulated galaxies with known similar morphologies to correct for the bias in low- $\langle \text{SNR} \rangle$ images. A similar approach would be to train a neural network on a set of deep or noise-free observations to mitigate observational biases (e.g., Jia et al. 2024). However, these solutions rely on assuming an intrinsic similarity between pairs or populations of galaxies, and therefore may disfavour finding rare objects with

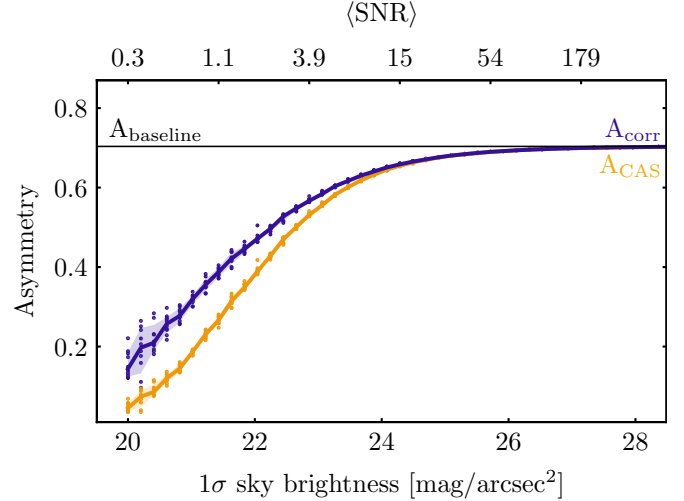


FIG. 4.— A_{CAS} (yellow) and A_{CAScorr} (purple) as a function of sky brightness or $\langle \text{SNR} \rangle$ for one simulated galaxy, compared to the baseline A_{CAS} (black). Both measurements significantly underestimate A_{CAS} up until $\langle \text{SNR} \rangle \sim 15$, although this threshold will change depending on the intrinsic asymmetry of the object (see Fig. 2). The scatter in points represents 10 different noise-realizations of the mock image, the solid lines represent their median, and the shaded regions span the 16th and the 84th quantiles.

high intrinsic asymmetries. On the other hand, Thorp et al. (2021) had previously suggested correcting for the noise dependency numerically, by fitting a polynomial to measured A_{CAS} , intrinsic A_{CAS} , and $\langle \text{SNR} \rangle$. This approach does not rely on having any prior knowledge of the object, although the fit itself needs to be calibrated for different algorithms and possibly datasets. Similarly, we provide an exponential fit to the relationship between observed and baselined A_{CAS} and $\langle \text{SNR} \rangle$; however, the scatter of this fit is larger for lower $\langle \text{SNR} \rangle$ values.

We suggest a third solution, which does not fully correct the measurement, but alleviates some of the noise dependence. We can re-define A_{CAS} as

$$A_{\text{CAScorr}} = \min_{\mathbf{x}_0} \frac{\sum_{ij} |I_{ij} - I_{ij}^{180}|}{\sum_{ij} I_{ij}} - \langle A_{\text{CAS},bg} \rangle. \quad (12)$$

where $\langle A_{\text{CAS},bg} \rangle$ is defined similarly to Eq. 2,

$$\langle A_{\text{CAS},bg} \rangle = \frac{N_{\text{ap}}}{N_{\text{sky}}} \frac{\sum_{ij}^{sky} |\epsilon_{ij} - \epsilon_{ij}^{180}|}{\sum_{ij} I_{ij}} \quad (13)$$

The only change from Eq. 1 is the normalization term, where the residual flux is normalized by the total flux, rather than the total absolute flux. This definition had been previously suggested in Schade et al. (1995), and used in practice (e.g., Yagi et al. 2006; Shi et al. 2009; Wen & Zheng 2016; Bottrell et al. 2024). With this definition, assuming the image is background-subtracted, the denominator is much more robust to changes in $\langle \text{SNR} \rangle$ and does not require any noise corrections. This means that A_{CAScorr} is independent of the aperture size like the noiseless A_{CAS} , making this measurement more robust.

The purple line in Fig. 3 shows that A_{CAScorr} flattens at the same radius as $A_{\text{CASbaseline}}$, as expected.

However, since the numerator is still affected by the noise flux, A_{CAScorr} will also produce biased asymmetry estimates. This is already seen in Fig. 3, but we show it more clearly in Fig. 4. Here we plot the measured asymmetry for the observed A_{CAS} and corrected A_{CAS} (yellow and purple respectively) as a function of the sky brightness for one galaxy. While A_{CAScorr} produces a less biased measurement than A_{CAS} , it is still significantly offset from the baseline value up to $\langle \text{SNR} \rangle > 15$. Moreover, this $\langle \text{SNR} \rangle$ threshold will change depending on intrinsic properties of the galaxy, as seen in Fig. 2. Thus, our noise-corrected A_{CAScorr} is not a solution to the noise dependence, but at least a way to obtain consistent measurements regardless of the aperture size or R_p definition on data with uniform depth.

3.2.4. Resolution dependence

The dependence on resolution stems from two factors. First, small-scale information is lost when it is discretized - any features smaller than the pixel scale cannot be recovered. Second, A_{CAS} also depends on the PSF size.

Let us consider a noiseless case, ignoring for the time being noise, discretization, and minimization. We can write the observed flux convolved with a PSF as $I(x) = \lambda * \mathcal{I}$. Then the observed asymmetry integral is

$$A_{\text{CAS}} = \frac{\int_{\mathbb{R}^2} |\lambda * (\mathcal{I} - \mathcal{I}^{180})| d\mathbf{x}}{\int_{\mathbb{R}^2} |\lambda * \mathcal{I}| d\mathbf{x}}. \quad (14)$$

Since λ and \mathcal{I} are positive for all \mathbf{x} , we can simplify the denominator using the fact that for any Lebesgue-integrable, strictly positive functions, $|f * g| = |f| * |g|$ and $\int_{\mathbb{R}^n} (|f| * |g|) = (\int_{\mathbb{R}^n} |f|)(\int_{\mathbb{R}^n} |g|)$. Since the integral of the PSF is 1, the denominator is invariant under convolution:

$$\int_{\mathbb{R}^2} |\lambda * \mathcal{I}| d\mathbf{x} = \left(\int_{\mathbb{R}^2} |\lambda| d\mathbf{x} \right) \left(\int_{\mathbb{R}^2} |\mathcal{I}| d\mathbf{x} \right) = \int_{\mathbb{R}^2} |\mathcal{I}| d\mathbf{x}. \quad (15)$$

On the other hand, the residual in the numerator is not invariant, since $\mathcal{I} - \mathcal{I}^{180}$ can be both positive and negative. In this case, by the triangle inequality, we have $|f * g| \leq |f| * |g|$, so

$$\int_{\mathbb{R}^2} |\lambda * (\mathcal{I} - \mathcal{I}^{180})| d\mathbf{x} \leq \int_{\mathbb{R}^2} |\lambda| * |\mathcal{I} - \mathcal{I}^{180}| d\mathbf{x} \quad (16)$$

$$= \int_{\mathbb{R}^2} |\lambda| d\mathbf{x} \int_{\mathbb{R}^2} |\mathcal{I} - \mathcal{I}^{180}| d\mathbf{x} \quad (17)$$

$$= \int_{\mathbb{R}^2} |\mathcal{I} - \mathcal{I}^{180}| d\mathbf{x}. \quad (18)$$

Combining the two, we can see that the asymmetry is underestimated:

$$A_{\text{CAS}} = \frac{\int_{\mathbb{R}^2} |\lambda * (\mathcal{I} - \mathcal{I}^{180})| d\mathbf{x}}{\int_{\mathbb{R}^2} |\lambda * \mathcal{I}| d\mathbf{x}} \quad (19)$$

$$= \frac{\int_{\mathbb{R}^2} |\lambda * (\mathcal{I} - \mathcal{I}^{180})| d\mathbf{x}}{\int_{\mathbb{R}^2} |\mathcal{I}| d\mathbf{x}} \quad (20)$$

$$\leq \frac{\int_{\mathbb{R}^2} |\mathcal{I} - \mathcal{I}^{180}| d\mathbf{x}}{\int_{\mathbb{R}^2} |\mathcal{I}| d\mathbf{x}} = A_{\text{CAStrue}} \quad (21)$$

Thus, even ignoring the loss of sub-pixel information, the measured asymmetry systematically decreases due to the PSF. The magnitude of this effect would depend on the relative sizes of the PSF and the asymmetric features. It is possible to correct for the PSF dependence with deconvolution (see Sec. 4.2), but the loss of the sub-pixel information is impossible to remedy analytically, although polynomial corrections may be tuned to particular observations (Thorp et al. 2021). One possible approach is to use machine learning and *infer*, rather than measure, the small-scale asymmetry. Such “super-resolution” techniques have recently gained popularity (e.g., Gan et al. 2021), but it is difficult to train them to correctly predict properties of rare objects, which are often the target of galaxy evolution studies.

4. RMS ASYMMETRY

RMS asymmetry, A_{RMS} , was first proposed in Conselice (1997) and Conselice et al. (2000), but did not become as widely used as A_{CAS} , since A_{CAS} correlated better with galaxy color in the Conselice et al. (2000) sample. However, as we showed in Sec. 3, the A_{CAS} measurement is extremely sensitive to noise due to its absolute-valued formulation, and here we show that A_{RMS} can alleviate this problem.

We define the true RMS asymmetry as:

$$A_{\text{RMStrue}}^2 = \min_{\mathbf{x}_0} \frac{\int_{-\infty}^{\infty} (\mathcal{I} - \mathcal{I}^{180})^2 d\mathbf{x}}{\int_{-\infty}^{\infty} \mathcal{I}^2 d\mathbf{x}} \quad (22)$$

and once again discretizing the measurement, we get the noiseless (but resolution-dependent) RMS asymmetry is:

$$A_{\text{RMSnoiseless}}^2 = \min_{\mathbf{x}_0} \frac{\sum_{ij} (\mathcal{I}_{ij} - \mathcal{I}_{ij}^{180})^2}{\sum_{ij} \mathcal{I}_{ij}^2}. \quad (23)$$

Just like for A_{CAS} , we tested the response of A_{RMS} to the changes in depth, pixel scale, and both, as shown left to right in Fig. 5. A_{RMS} is invariant to changing $\langle \text{SNR} \rangle$ down to $\langle \text{SNR} \rangle \sim 1$, and is independent of the aperture size. However, A_{RMS} is more affected by changes in resolution - similarly to A_{CAS} , A_{RMS} is underestimated in images with worse resolution in a way that depends both on the resolution, and the intrinsic asymmetry.

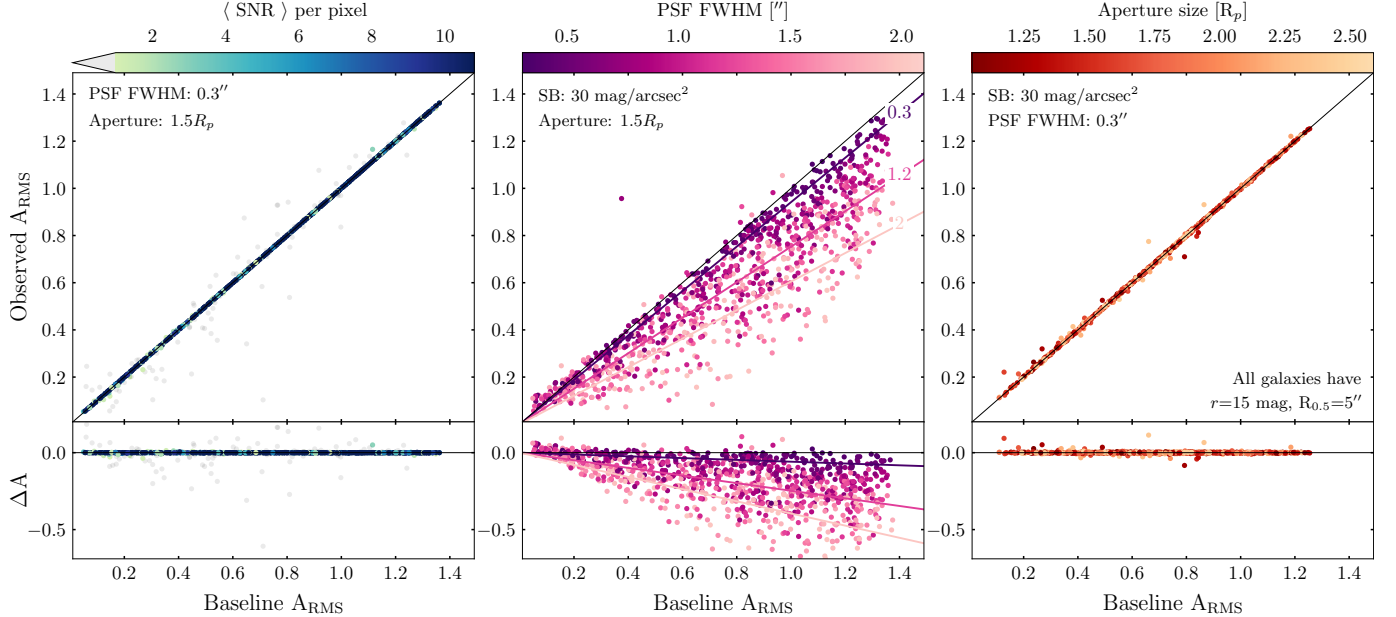


FIG. 5.— Same as Fig. 2, showing the test results for the A_{RMS} measured on the mock observation (y-axis) and the baseline image (x-axis). A_{RMS} is independent of $\langle \text{SNR} \rangle$ as long as $\langle \text{SNR} \rangle > 1$. Similarly, since noise does not affect the measurement, A_{RMS} is independent of the aperture size. However, A_{RMS} has a stronger resolution dependence than A_{CAS} , significantly underestimating asymmetry for PSF FWHM $> 1''$.

4.1. Robustness to noise

For most $\langle \text{SNR} \rangle$ regimes, A_{RMS} perfectly recovers the true asymmetry. This is because the square of flux is mathematically better-behaved than the absolute value of flux, allowing us to separate out the source and noise contributions to the sum.

As before, let us assume that the noise is purely Gaussian and originates from the background, and ignore the effects of the PSF or minimization. Since $\mathcal{I} = I + \epsilon$, we can write the observed A_{RMS} as

$$A_{\text{RMS obs}}^2 = \frac{\sum_{ij} (I_{ij} - I_{ij}^{180})^2}{\sum_{ij} I_{ij}^2} \quad (24)$$

$$= \frac{\sum_{ij} ((\mathcal{I}_{ij} - \mathcal{I}_{ij}^{180}) + (\epsilon_{ij} - \epsilon_{ij}))^2}{\sum_{ij} (\mathcal{I}_{ij} + \epsilon_{ij})^2}. \quad (25)$$

Since the source flux and the noise are uncorrelated in our approximation, and the noise is Gaussian with zero mean, $\langle \mathcal{I}_{ij} \epsilon_{ij} \rangle = 0$, so the cross-terms vanish and this equation simplifies to

$$A_{\text{RMS obs}}^2 = \frac{\sum_{ij} (\mathcal{I}_{ij} - \mathcal{I}_{ij}^{180})^2 + 2\sigma_{\text{sky}}^2}{\sum_{ij} \mathcal{I}_{ij}^2 + \sigma_{\text{sky}}^2}. \quad (26)$$

Therefore, we can recover the true A_{RMS} from the observed image as

$$A_{\text{RMS noiseless}}^2 = \frac{\sum_{ij} (I_{ij} - I_{ij}^{180})^2 - 2\sigma_{\text{sky}}^2}{\sum_{ij} I_{ij}^2 - \sigma_{\text{sky}}^2}. \quad (27)$$

Of course, we have made a number of assumptions, most importantly that the background noise is flat and

well-described by $\mathcal{N}(0, \sigma_{\text{sky}}^2)$. In reality, we can compute the background contribution to asymmetry more robustly, as described in Appendix B. However, the important advantage of this approach is that the background contribution to asymmetry is completely separable, and thus we can recover the baseline asymmetry, as seen in the first panel of Fig. 5. We do not fit any relationship between the observed and the baseline A_{RMS} , since it is clear from the plot that the asymmetry is recovered perfectly up until $\langle \text{SNR} \rangle$ reaches 1.

4.2. Resolution matching

While A_{RMS} is a very robust measurement for varying noise levels, it depends on the resolution more than A_{CAS} , as seen in the middle panel in Fig. 5. The reasons for this dependence are the same as for A_{CAS} , which we described in Sec. 3.2.4. As we decrease resolution, we are able to resolve fewer small-scale features of the image, and thus the overall asymmetry decreases. The impact of the PSF is stronger in the case of A_{RMS} , since it redistributes the flux away from the brightest regions, reducing the total sum of squared fluxes. The best-fit relationship between A_{RMS} and the PSF size is exponential:

$$A_{\text{RMS obs}} = A_{\text{RMS base}} \exp \left[- \left(\frac{\text{PSF FWHM}}{3.7} \right)^{-1.1} \right] \quad (28)$$

The resolution dependence then has two roots: due to PSF smearing and due to loss of sub-pixel information. It is possible to remedy the PSF effect, but not the discretization one – we cannot recover the lost information

on individual galaxies. Therefore, it is important to recognize that both A_{CAS} and A_{RMS} are *not scale-invariant*, and it is only meaningful to compare asymmetries calculated for a given physical size.

However, we can improve the calculation by matching the resolution of the observed image to the baseline resolution. While it is not possible to recover sub-pixel features, we can remove the effect of the PSF. To do this, we rescale our mock images to the baseline pixel scale ($0.1''$) using linear interpolation. In practice, this scale should be defined using a physical size of features of interest in pc. Since our galaxies are simulated to match $z \approx 0.1$ observations, this pixel scale maps 200 pc features. Note that although the mock observations are now sampled on a fine pixel scale, any information that was originally unresolved is still lost since interpolation cannot recover it. After rescaling the images, we deconvolve them.

In general, deconvolution is a complicated task. Since several intrinsic light distributions can produce the same image under convolution, the inverse is ill-defined when the image is noisy. There are many proposed deconvolution algorithms, some simpler and some more complex. Among the current state-of-the-art solutions are: 1) using machine learning-based techniques to achieve super-resolution (e.g., Gan et al. 2021) and 2) optimizing the deconvolved image numerically (e.g., Shibuya et al. 2022; Michalewicz et al. 2023; Millon et al. 2024). However, both approaches have limitations. Neural network techniques typically have to be trained on a large dataset (although pre-training or self-supervised approaches can remedy this), and generally underperform on rare objects, such as disturbed galaxies, making this method less suitable for detecting asymmetries. On the other hand, numerical optimization techniques do not rely on the training data, but take a long time to converge for individual galaxies and so are difficult to apply to large survey datasets.

In this work, we opted for a simpler and faster approach to deconvolve images directly in Fourier space. We use a transform similar to Wiener deconvolution (Wiener 1949), which combines the PSF deconvolution with a noise-damping term. Our approach differs in that we aim to recover a *noisy* deconvolved image to avoid denoising artifacts, and it is described in detail in Appendix C. Similarly to Cantale et al. (2016), instead of deconvolving the image completely, we deconvolve it down to a narrow Gaussian PSF (3 pixels FWHM) to ensure the final image is Nyquist-sampled. Our resolution-matched images are then produced in the following way: we rescale the image to the desired pixel scale ($0.1''$) using linear interpolation, and then apply the transformation in Fourier space to deconvolve the observed image and recover the Nyquist-sampled noisy source image.

Fig. 6 shows the relationship between the baseline

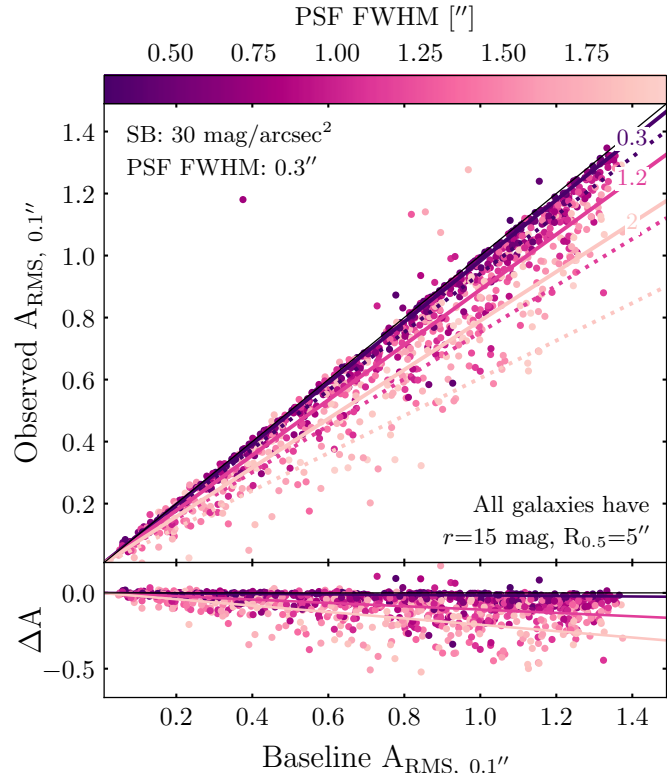


FIG. 6.— Same as the middle panel of Fig. 5, showing the resolution dependence of resolution-matched A_{RMS} . Here, the mock images were upsampled and deconvolved to match the baseline resolution of $0.1''$. The solid lines show the best fit for the PSF size dependence for $0.3''$, $1.2''$, and $2''$ PSFs. The dashed lines show the corresponding fits for the simple A_{RMS} measurement without a resolution correction. While some resolution-dependent bias persists, it is reduced compared to the original A_{RMS} .

A_{RMS} and the resolution-matched $A_{\text{RMS},0.1''}$. We omitted the $\langle \text{SNR} \rangle$ and the aperture size series from this plot since resolution matching does not affect the results. Again, the best fit for the dependence on the PSF size is exponential, but with a smaller offset for a given resolution:

$$A_{\text{RMS,obs}} = A_{\text{RMS,base}} \exp \left[- \left(\frac{\text{PSF FWHM}}{5.7} \right)^{-1.4} \right] \quad (29)$$

we show the best fit lines for three different PSF sizes in Fig. 6 as solid lines, and the best fit lines for the uncorrected A_{RMS} measurement as dashed lines of the same color. As seen in the figure, the resolution correction reduces the measurement bias, although A_{RMS} is still underestimated when the mock PSF is much larger than the baseline. The offset from the baseline measurement is large for $\text{PSF FWHM} > 2''$, five times wider than the best-case PSF. As we discussed, although deconvolution can remedy the impact of the PSF on the flux distribution, it cannot recover the subpixel information, so providing a complete correction without making any inferences about the underlying lost structure is impossible.

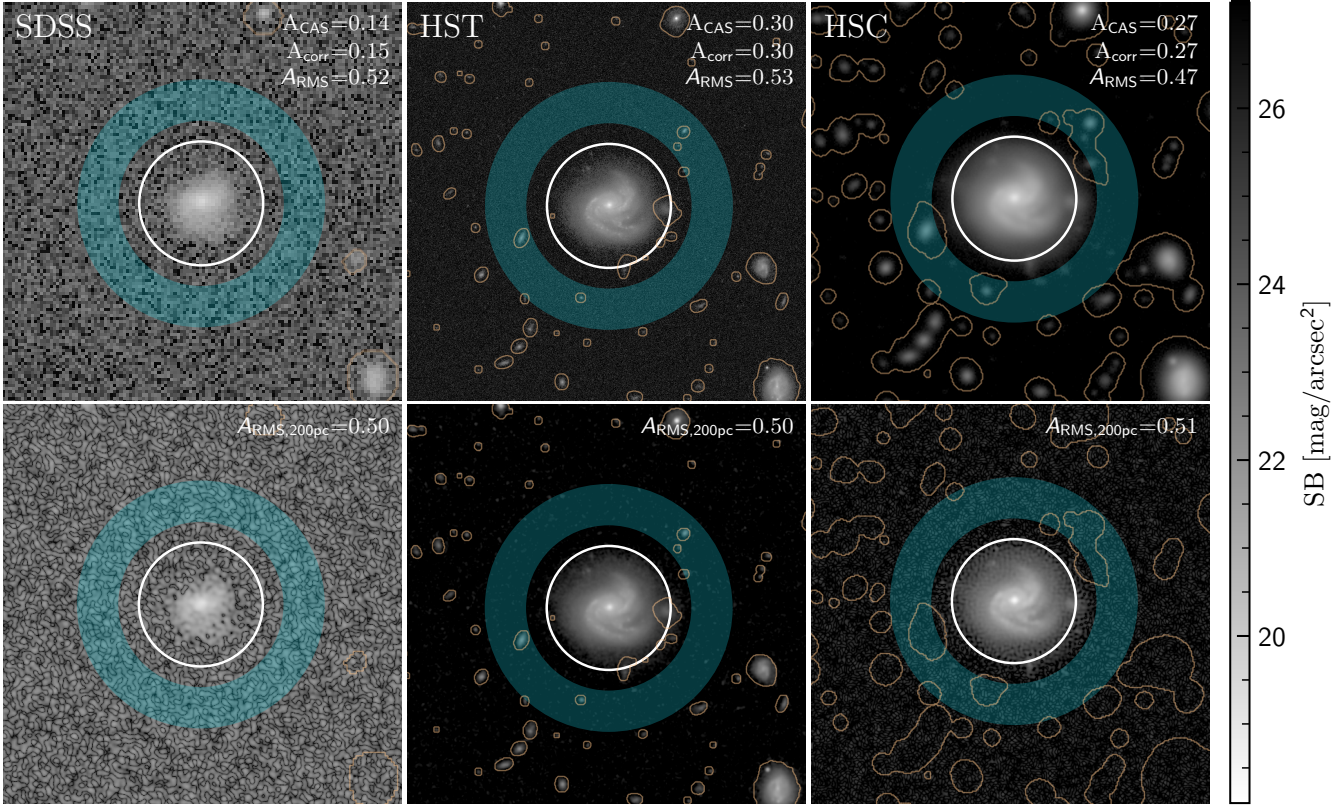


FIG. 7.— An example galaxy observed with SDSS (left), *HST* (center), and HSC (right) in the *I*-band filter or equivalent. The **top** row shows the pipeline-reduced images and A_{CAS} , A_{CAScorr} , and A_{RMS} measurements. Foreground objects were masked (thin orange contours), and all asymmetry metrics were calculated within $1.5R_p$ (white solid circle). Sky asymmetry was estimated in a $2-3R_p$ annulus (blue region). The **bottom** row shows resolution-matched images: SDSS and HSC observations were both upscaled and deconvolved down to 200 pc/px resolution, and the *HST* image was downsampled and convolved with a 3-pixel-wide Gaussian PSF. The spiral structure is visibly sharper after deconvolution, and the deconvolved HSC image is visually similar to the *HST* one. While both A_{CAS} and A_{RMS} measurements show an inconsistency between at least one pair of observations, $A_{\text{RMS},200\text{pc}}$ measurements are consistent between all three.

5. A PILOT TEST ON OBSERVED DATA

In this section, we present the tests of all the asymmetry measurements against a pilot dataset of real observed. While simulations can show general trends in performance, they cannot test the robustness of our metric to different artifacts, non-Gaussian noise, or real asymmetric features, and so we turned to observational data.

For this test, we used the sample from Sazonova et al. (2021), who studied disturbances in post-starburst galaxies at $z \approx 0.1$. They constructed stellar mass and redshift-matched samples of quiescent, star-forming, and post-starburst galaxies that are observed with the *HST* and SDSS in the same filters. We selected 27 galaxies from the sample that also have *i*-band HSC observations. While this is a small dataset, it spans a selection of mass- and redshift-matched star-forming, quiescent, and post-starburst / post-merger galaxies, and therefore a large range of intrinsic asymmetries. This dataset is an ideal test sample to evaluate the dependence of asymmetry measurements on both resolution and signal-to-noise ratio: it provides deep, high-resolution observations from *HST*, deep but lower-resolution observations from HSC, and shallow low-resolution observations from

SDSS. The observations were all taken in similar filters (*I*-band or equivalent), so there are no intrinsic differences between observed galaxy structures. Therefore, a perfect A measurement should produce the same result for a given galaxy for all three instruments. A table providing some basic properties of this sample (mass, redshift, and depths of each image) as well as all asymmetry measurement is provided in Appendix D.

5.1. Data processing

Before calculating asymmetry, we needed to process the images. The SDSS observations were obtained from the SDSS Science Archive Server³ (Blanton et al. 2017), and the HSC ones from the Image Cutout service of the HSC Subaru Strategic Program⁴ (Aihara et al. 2022). These observations were already reduced by their respective standard pipelines. The *HST* data was obtained as part of a snapshot proposal (Proposal 14649; PI Alatalo), and reduced as described in Sazonova et al. (2021). The images were used to create 40'' cutouts centered on each galaxy in the sample. An example galaxy observed

³ SDSS DR16 Science Archive Server – dr16.sdss.org

⁴ HSC SSP Data Access

with all three instruments is shown in Fig. 7 (top row) with the SDSS image on the left, *HST* in the center, and HSC on the right.

Next, we needed to mask all extraneous sources on the image and calculate the Petrosian radius. We opted to do this independently for each image. This choice can, in theory, add some differences in measured parameters: faint sources that are not masked in shallow observations can add to background asymmetry and thus affect our results. However, this is the most realistic set-up, as in most cases a deeper image is not available to construct the mask.

We followed the 3-step segmentation routine from Sazonova et al. (2021). This algorithm uses PHOTUTILS to construct three segmentation maps – “hot”, “cool”, and “cold” – and combine these maps into one map that aims to both capture faint envelope of the main source, and mask sources outside of the galaxy or bright foreground clumps within the galaxy. We grew the resulting mask by 5% of the image size to capture any remaining faint contaminant light. Masked sources are shown with thin orange contours in Fig. 7. We then used PETROFIT (Geda et al. 2022) to calculate the Petrosian radius independently for each images. In Fig. 7, we show the $1.5R_p$ region in which asymmetry is calculated as a solid white circle, and a sky region corresponding to $2\text{--}3R_p$ as a blue annulus.

Since we showed that both asymmetry measurements depend on resolution, we also calculate a resolution-matched $A_{\text{RMS},200\text{pc}}$ by rescaling all images to a pixel scale that corresponds to 200 pc per pixel. We do this by finding the angular resolution that corresponds to this physical resolution at the redshift of each object. The resulting pixel scale for each image is shown in Appendix D. For all galaxies, this resolution is higher than either that of HSC and SDSS, so we deconvolved these images as described in Sec. 4.2. On the other hand, *HST* has a finer resolution, so we downsampled the *HST* images to the required pixel scale and convolved them with a 3-pixel Gaussian PSF to ensure Nyquist sampling. While this means some of the information in the *HST* images was lost, the $A_{\text{RMS},200\text{pc}}$ measurement requires a uniform spatial resolution, and we could not resample the shallow SDSS images any finer since resampling decreases $\langle \text{SNR} \rangle$ below 1. In general, it is not feasible to upscale observations by more than a factor of a few, since both the $\langle \text{SNR} \rangle$ decreases in the process, and smaller-scale features that are unresolved on the original pixel scale cannot be recovered anyway. Therefore, we opted for a matched resolution of 200 pc, which can capture asymmetries such as large star-forming regions, spiral arms, dust lanes, and tidal tails. The bottom panel of Fig. 7 shows the resolution-matched *HST*, HSC, and SDSS images. As seen in the image, our deconvolution routine

(Appendix C) sharpens the spiral structure in ground-based observations; most strikingly, the HSC image after deconvolution is visually very similar to the *HST* image sampled on the same pixel scale.

5.2. Performance of asymmetry metrics

For each galaxy and each instrument, we measured four asymmetries: A_{CAS} , corrected CAS asymmetry A_{CAScorr} , RMS asymmetry A_{RMS} , and resolution-matched $A_{\text{RMS},200\text{pc}}$. The results for our sample are shown in Fig. 8. The figure is split as follows: we plotted A_{CAS} and A_{CAScorr} in the top row (yellow and purple, respectively), while A_{RMS} and $A_{\text{RMS},200\text{pc}}$ are in the bottom row (yellow and purple). On each panel, we plotted asymmetry of each galaxy measured with one instrument on the x-axis and another on the y-axis. The solid black line indicates a 1-to-1 agreement between the instruments. For each set of measurements, we also calculated the best-fit gradient, computing the 1σ uncertainty on the gradient via bootstrapping. A gradient close to one indicates that the measurements between two datasets are consistent, whereas a shallower or a steeper gradient indicates a bias.

Looking at the top row, we see again evidence for the dependence of A_{CAS} on image depth. The measurements are consistent between *HST* and HSC observations (middle panel) – which are both very deep. On the other hand, neither *HST* nor HSC agree with shallower SDSS observations. We also see a strong dependence on the intrinsic asymmetry: more disturbed galaxies have a higher measurement bias in SDSS, as seen by the shallow best-fit gradients. As a result, asymmetry measurements made using SDSS will have a much lower dynamic range, and thus are unable to differentiate truly undisturbed galaxies from weakly disturbed ones. A_{CAScorr} shows the same error as A_{CAS} , which is expected from our tests, since A_{CAScorr} corrects the dependence of A_{CAS} on the aperture size but not overall $\langle \text{SNR} \rangle$ -dependent bias (see Fig. 3).

On the bottom row, we see a much better agreement between SDSS, *HST*, and HSC. For the simple A_{RMS} measurement, the results are consistent between SDSS and HSC (which have more comparable resolution), but there is a shallow slope indicating a bias comparing to *HST* observations. On the other hand, for the resolution-matched $A_{\text{RMS},200\text{pc}}$ measurement, in all three cases the slope is consistent with one, indicating no bias when comparing the results between three different instruments. However, there is a significant scatter around the one-to-one line, with a root-mean-squared error of 0.06–0.09. The scatter represents various observational uncertainties that are not present in the simulated dataset: the difference in masking of foreground and background sources between images, artifacts that can affect the measure-

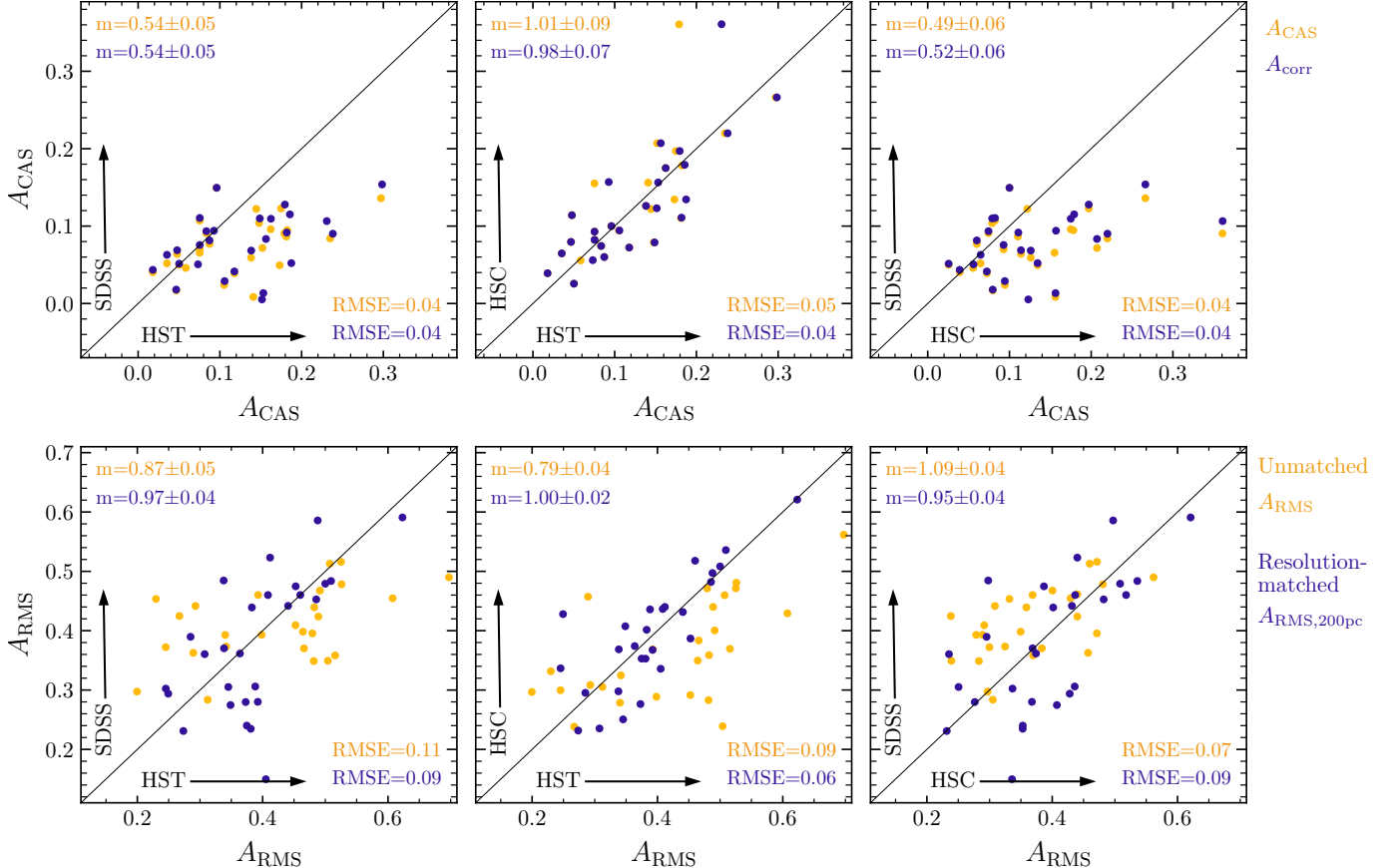


FIG. 8.— A comparison of asymmetry measured between pairs of observations of the same galaxies for A_{CAS} metrics (A_{CAS} and A_{CAScorr} , **top**), and A_{RMS} metrics (A_{RMS} and $A_{\text{RMS},200\text{pc}}$, **bottom**). The comparisons are between SDSS and HST (**left**), HSC and HST (**center**), and SDSS and HSC (**right**). The diagonal line shows a one-to-one relationship, or an agreement between the metrics measured on two different images. The slope of the line of best fit for each sample is shown in the top-left, where a slope close to 1 indicates a good agreement and a shallower/steeper slope indicates a measurement bias. The root-mean-square error compared to the best fit is shown in the bottom right. A_{CAS} is systematically underestimated in shallow images compared to deep ones (SDSS/ HST and SDSS/HSC), but is consistent in images of similar depth (HSC/ HST). Meanwhile, $A_{\text{RMS},0.1''}$ provides consistent measurements for all three instruments, albeit with a large scatter around the diagonal, indicative of uncertainties in the asymmetry measurement.

ment, the slightly variable R_p , and the challenging nature of deconvolution. However, the scatter is not biased in either direction, making resolution-matched A_{RMS} an overall more robust metric. Instead, we can interpret this scatter as the expected uncertainty of each asymmetry measurement when comparing catalogs made with different observational datasets, particularly where the native pixel scales are very different.

6. DISCUSSION

6.1. Asymmetry & noise

In this work, we aimed to understand why asymmetry measurements depend so strongly on imaging quality. We studied how four metrics depend on noise and resolution: A_{CAS} , a noise-corrected A_{CAScorr} , a root-mean-square A_{RMS} , and a resolution-matched $A_{\text{RMS},0.1''}$ (or $A_{\text{RMS},200\text{pc}}$, where the resolution limit is defined in terms of a physical scale).

In Section 3, we showed that the dependence of A_{CAS} on image depth arises due to a nonlinear dependence of the absolute-valued function on the noise term. In

the extremely high signal-to-noise ratio regime, the noise contribution to the total flux is low, and therefore A_{CAS} is a reliable metric, although even when $\langle \text{SNR} \rangle$ is high, A_{CAS} may be negative if the source is intrinsically very *symmetric* (see Sec. 3.2.1).

In shallower imaging, noise always contributes to the measurement despite the background asymmetry correction term. It adds bias both in the numerator of the equation (the asymmetry residual) and the denominator (the normalization flux), which leads to two issues: first, asymmetry is always systematically underestimated when noise is present; second, the measurement is highly dependent on aperture size as more sky pixels are added to the normalization flux. One easy correction that can be made is normalizing asymmetry with the total photometric flux, rather than the total absolute flux (using A_{CAScorr} , Sec. 3.2.3), thereby reducing the noise contribution to the normalizing flux. This correction remedies the aperture size and inclination dependence, but still provides biased estimates when $\langle \text{SNR} \rangle$ is varied.

In Section 4, we studied a similar metric: a root-mean-

Use case

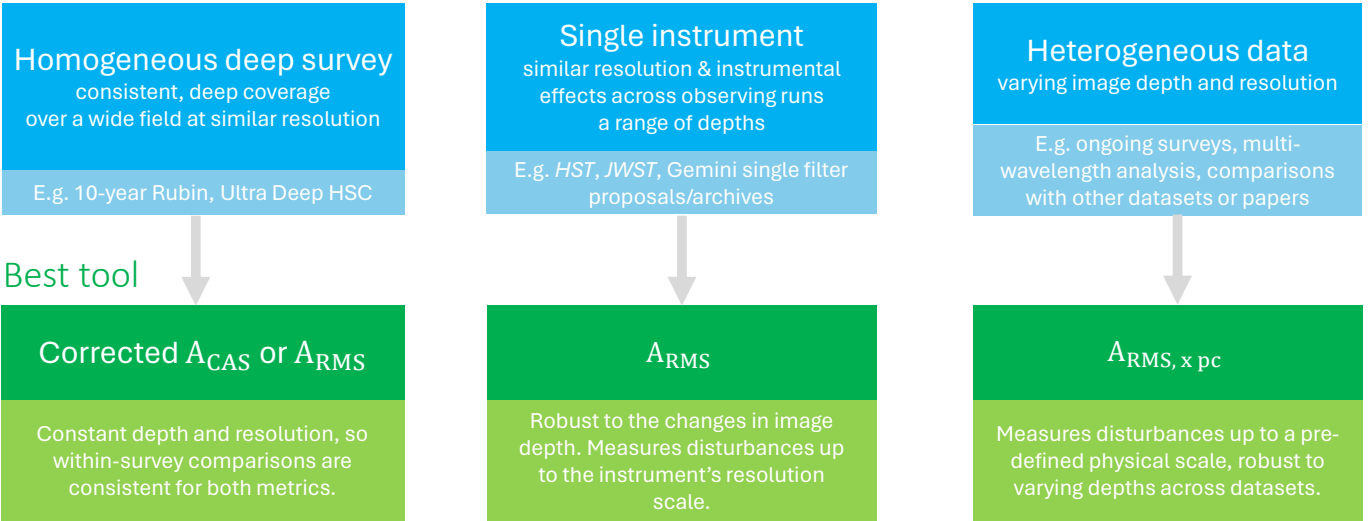


FIG. 9.— A schematic guidance on the the best asymmetry metrics for different studies, depending on the data type and origin. In general, $A_{\text{RMS}, x \text{ pc}}$ will provide the most robust measurements while enabling comparisons across different experimental or redshift regimes.

square asymmetry, A_{RMS} . The idea of measuring asymmetry of the squared flux distribution was first introduced in Conselice et al. (2000) alongside the commonly used A_{CAS} , however it never gained popularity. At various times, it was re-proposed (e.g., Deg et al. 2023), but to this day an A_{RMS} measurement has not gained traction. In this work, we looked at the behaviour of A_{RMS} in more detail to compare it to A_{CAS} . We opted for a root-mean-square asymmetry, rather than a squared one, so that the strength of disturbances grows linearly rather than quadratically.

We showed that A_{RMS} is extremely robust to a changing signal-to-noise ratio, since the noise term easily decouples from the calculation in the assumption of uncorrelated Gaussian noise, above $\langle \text{SNR} \rangle > 1$, and remains robust in realistic images with complex sky backgrounds (Section 5). The measurement scatter increases in extremely shallow imaging due to instabilities in the minimization step. We note that it may be possible to skip minimization (see Appendix A), which we will explore in a future work.

6.2. Asymmetry & resolution

Both A_{CAS} and A_{RMS} are sensitive to image resolution, but this sensitivity is more extreme for A_{RMS} . This leads to a more philosophical discussion of the nature of the *intrinsic* asymmetry of an object. Regardless of a computational strategy, asymmetry is defined as the difference between flux distributions under a rotation by 180° . At infinite resolution, galaxies will possess many small-scale asymmetric features: star clusters, gas clouds, and even individual stars, leading to a high asymmetry value under this definition. This is a similar argument to that of measuring the length of a coastline (e.g., Mandelbrot 1967): with increasing resolution levels, more irregular

features appear, increasing the total length – in that sense, galaxies, as a coastline, are fractal objects and thus a resolution-independent asymmetry value is impossible to define. Instead, just like with other fractal objects, it is useful to define a metric at a given resolution. Ideally, this resolution should be chosen as the physical scale of the disturbance we would like to detect.

In this work, we devised a new Fourier-based deconvolution approach to match the resolution of different observations (see Appendix C). Our method is quick, but more robust methods exist – for example, starlet deconvolution that uses optimization to find the best final image (Michalewicz et al. 2023). For the analysis of large survey data, we recommend using Fourier deconvolution as it is significantly faster, but optimization techniques should yield better results.

Accounting for this resolution dependence, we defined a new measurement, $A_{\text{RMS}, x''}$ ($A_{\text{RMS}, x \text{ pc}}$), or RMS asymmetry measured at a spatial resolution of x arcseconds (x parsec). For the observed dataset, we calculated $A_{\text{RMS}, 200 \text{ pc}}$, RMS asymmetry resolved at 200 pc. At this resolution, we can detect large asymmetric features such as tidal tails, as well as disturbances to the spiral structure and relatively small satellite galaxies, but we do not resolve individual stellar clusters, so they do not contribute to the measured asymmetry.

Our new metric is able to provide consistent asymmetry measurements independently of image depth, after the observations are resampled and (de-)convolved to match the desired resolution. However, there are two caveats. First, during upsampling, low-resolution observations lose effective $\langle \text{SNR} \rangle$. Therefore, with shallow observations such as that of SDSS, it is impossible to measure asymmetry on finer scales than those we

tested in this work due to the loss of SNR. Our deconvolution approaches also dampens the noise-dominated high-frequency terms, so the effectiveness of deconvolution falls with decreasing $\langle \text{SNR} \rangle$. Second, it is impossible to recover features that are much smaller than the original pixel scale since upsampling simply interpolates between pixels – it is thus important to find a balance between the desired resolution and one that the instrument is capable of reaching. We chose 200 pc for our tests as this required us to upsample SDSS images by a maximum factor of four, and allowed us to resolve structures where asymmetries can provide information about physical structures such as spiral arms and satellites.

The resolution dependence is especially important to keep in mind when comparing the structure of galaxies across different cosmic times. If galaxies observed in the same survey are located at different redshifts, the effective spatial resolution of these galaxies will change depending on their distance from us. Therefore, there will be a redshift-dependent bias in simple A_{CAS} and A_{RMS} measurements that may be misinterpreted as evolution of the “disturbance”, when in fact, the disturbance of different features is probed at these different scales. Our new $A_{\text{RMS,}x\text{pc}}$ measurement will probe the asymmetry of the same physical features, regardless of the object’s redshift, and therefore allow a more consistent analysis.

However, care must still be taken when comparing galaxies of different physical sizes. In smaller or lower-mass galaxies, some features such as spiral arms may also be smaller; so even a physically-motivated asymmetry may be probing different *types* of features. However, not all features may have this size dependence: e.g., the size of the tidal tails depend more on the orbit and the stage of the merger than the size of the host. This analysis is beyond the scope of this paper, but may warrant further study.

6.3. Detecting galaxy mergers

One advantage of the $A_{\text{RMS,}x\text{pc}}$ metric is that is independent of image properties, and provides consistent results at any redshift. While traditionally $A_{\text{CAS}} > 0.3$ has been used as a threshold above which a galaxy is considered “disturbed”, this threshold will vary for datasets with different image properties. On the other hand, since $A_{\text{RMS,}x\text{pc}}$ does not strongly depend on resolution or depth, such a threshold would be more universal, and we plan to determine the range of $A_{\text{RMS,}x\text{pc}}$ typical of disturbed galaxies in a future study with a larger sample.

However, simply using a disturbance threshold to detect merging galaxies is not effective, since the observed morphology of a merging pair depends strongly on the merger stage, properties of the galaxies, and their or-

bits (e.g., Pawlik et al. 2016). Some mergers may have a detectable asymmetry while others may not: for example, late-stage mergers in early-type galaxies are seen as shells, an inherently symmetric feature. Selecting merger candidates using asymmetry alone will not provide either a pure or a complete sample (e.g., Thompson et al. 2015; Bignone et al. 2017; Wilkinson et al. 2024).

If the goal is to obtain the most pure and/or complete merger sample, modern deep learning techniques ubiquitously outperform an “asymmetry threshold” approach (e.g., Ackermann et al. 2018; Bottrell et al. 2019; Domínguez Sánchez et al. 2023). The advantage of quantitative morphology metrics, however, is their interpretability and versatility. Different metrics probe different types of disturbances, and can be used in tandem to easily tailor the selection to a particular class of galaxies (e.g., mergers of different stages; Snyder et al. 2015; Nevin et al. 2019). To do this effectively, it is important to consider the types of features each metric is sensitive to.

Since both A_{CAS} and A_{RMS} are flux-weighted, they are more sensitive to bright disturbances rather than low-surface brightness features such as tidal tails. A_{RMS} scales the residual flux quadratically, and so is even more biased towards bright pixels. Therefore, this metric is sensitive to internal asymmetries, such as star-forming clumps, double nuclei, or prominent dust lanes. This means that A_{RMS} is best-suited for detecting mergers before the two cores coalesce. Moreover, the flux weighting means asymmetry may be better at detecting major mergers (Nevin et al. 2019), although Bottrell et al. (2024) show that a significant fraction of asymmetries are induced by minor and micro-mergers. On the other hand, shape asymmetry defined in Pawlik et al. (2016) is not flux-weighted, and so is sensitive to large-scale faint features, such as tidal tails. Combining A_{RMS} and shape asymmetry will allow probing both the internal and tidally induced disturbances caused by the merger – this will be tested on a large dataset in a future study.

Finally, asymmetry is a good metric to probe asymmetries that are unrelated to mergers, such as those caused by clumpy star formation and/or dust absorption (e.g., Sazonova et al. 2021); however, the relative magnitude of asymmetries induced by these features needs to be established on a large dataset.

6.4. Considerations for surveys, pipelines, and catalogs

While no measurements are able to perfectly reproduce the intrinsic asymmetry regardless of the imaging properties, they individually excel in different scenarios. We provide guidance on the performance of different metrics studied in this work in Fig. 9, to aid future analysis, survey, and pipeline design.

In deep, homogeneous surveys, if the variations in image depth and resolution are minimal, both A_{CAS} and

A_{RMS} can be used to obtain consistent asymmetry measurements within that survey area. However, in many surveys, depth can vary significantly (e.g., in HSC COSMOS field, the depth varies by 2 magnitudes; [Aihara et al. 2022](#)). If variations in seeing are less significant than variations in depth, A_{RMS} will provide more consistent results. If using A_{CAS} , we recommend using the new corrected $A_{\text{CAS,corr}}$ with a non-absolute denominator term to reduce the noise-dependence. As shown in Sec. [3.2.3](#), the corrected A_{CAS} measurement does not depend on aperture size, and therefore will be more robust to changing numerical implementations. Deep surveys such as the HSC Ultra Deep field or the upcoming Rubin LSST will both provide reliable A_{CAS} and A_{RMS} measurements.

In shallow surveys A_{RMS} will outperform A_{CAS} since A_{CAS} depends non-linearly on the intrinsic asymmetry. This means that the dynamic range of A_{CAS} is small in surveys such as SDSS and Pan-STARRS, and only extremely disturbed objects can be identified as asymmetric. For example, [Rodriguez-Gomez et al. \(2019\)](#) show that most galaxies in the Pan-STARRS survey have $A_{\text{CAS}} < 0.1$, with only a few galaxies identified as mergers. This low dynamic range can lead to us to underestimate the role of structural disturbances and mergers in galaxy evolution (e.g., [Sazonova et al. 2021](#); [Wilkinson et al. 2024](#)).

For data obtained with a single instrument outside of a survey, e.g. as part of a proposal or an archival search, A_{RMS} will be the more robust measurement. The resolution of a single space-based instrument is essentially constant while exposure times differ depending on the observational program, so A_{RMS} is the better choice. For ground-based instruments, the seeing varies more, but the variations are still typically within $0.1\text{--}0.3''$, while resulting depth can vary a lot more significantly.

In general, astronomers would like to be able to compare our data to data obtained by other scientists, instruments, or surveys. Astronomical data are extremely heterogeneous both in terms of resolution and depth: it depends on the instrument, the filter, the weather conditions, the choice of the observing strategy, and more. Objects with different redshifts will necessarily have different physical resolution when observed with a single instrument. Therefore, for most applications, we recommend using $A_{\text{RMS,x pc}}$ - RMS asymmetry at a given spatial resolution. Ideally, the spatial resolution should depend on the physical scale of the disturbances. In this work, we used $A_{\text{RMS,200pc}}$, which will be a good choice for most applications studying global structural evolution of galaxies, since it captures the largest star-forming regions, spiral structure, and tidal perturbations, while not accounting for the intrinsically asymmetric distribution of the individual star-forming clumps in the galaxies.

The implication of this new approach is that some high-resolution imaging, such as that obtained by *HST* and *JWST*, will need to be *downgraded* to match the coarser resolution of $A_{\text{RMS,200pc}}$. While initially this sounds contentious, it is crucial to remember that the asymmetry metric is resolution-dependent by design, and so the physical scale of the features we wish to analyze needs to be set. With the resolution limit fixed, observers will still need to ensure that the observations they use for their measurements are rescaled to the corresponding pixel scale, which will depend on the redshift of the object. With these considerations, our advice for observers and pipeline developers who wish to provide the community with morphology catalogs that include asymmetry is the following:

1. Compute both A_{CAS} and A_{RMS} on the reduced images, since these metrics are easiest to interpret and will be robust within the survey volume.
2. Compute $A_{\text{RMS,0.1''}}$ on images rescaled to $0.1''$, since this is a pixel scale that traces meaningful physical features for $z < 2$ galaxies, and is attainable through deconvolution for most other surveys, including SDSS. This pixel scale is approximately the same as the native pixel scale of Euclid, Roman, and *JWST*, and is easily achievable for LSST through upsampling by a factor of 2.
3. Encourage users to use re-compute a physically-motivated $A_{\text{RMS,200pc}}$ measurement for their own datasets, especially when considering the evolution of asymmetry across cosmic time.

Finally, some of the issues outlined here can be resolved with machine learning. For example, [Desmons et al. \(2023\)](#) and [Vega-Ferrero et al. \(2024\)](#) trained a model that can be used in the future to classify galaxies independently of the noise level by including noise augmentations during training, while [Tohill et al. \(2021\)](#) developed a neural network that predicts the CAS concentration, asymmetry, and smoothness simultaneously, giving a 10,000 speed-up compared to an analytical computation. Combining the two approaches could help mitigate the noise-dependence of A_{CAS} . However, neural networks perform worse on rare objects (such as mergers) as they are often under-represented in training sets, unless specifically tuned to be sensitive to those features, in which case they can over-predict the number of disturbed objects. Moreover, it is beneficial to use a metric that is initially defined to be better-behaved, such as $A_{\text{RMS,x pc}}$, and then train a model to predict this metric in an automated way.

7. SUMMARY

We have tested the performance of four asymmetry measurements: A_{CAS} (Conselice et al. 2000), a corrected $A_{\text{CAS,corr}}$ with a better normalization, root-mean-squared A_{RMS} (Conselice et al. 2000), and $A_{\text{RMS,200 pc}}$ ($A_{\text{RMS,0.1''}}$) calculated on images with matched resolution of 200 pc (0.1'') per pixel. We evaluated these metrics on a set of simulated GALSIM galaxies with varying image depth and resolution, as well as on a set of 27 galaxies observed with *HST*, SDSS, and HSC in the *I*-band.

Our main results are:

1. **A_{CAS} severely underestimates asymmetry in shallow images** due to its absolute-valued definition (Sec. 3.2.1). The bias grows exponentially with decreasing $\langle \text{SNR} \rangle$, and is large for images with SNR per pixel less than 5.

Asymmetry of disturbed objects is affected more, leading to a lower overall dynamic range of A_{CAS} in shallow surveys. Therefore, disturbed galaxies will have similar A_{CAS} values to regular ones, making them difficult to identify.

Another side effect of the noise impact is that A_{CAS} depends on the aperture size. We provided a simple correction that alleviates the aperture size dependence (Sec. 3.2.3).

2. **A_{RMS} is insensitive to image depth** (Sec. 4). Due to defining A_{RMS} as a square of the residuals, the background contribution can be easily subtracted, making this metric incredibly robust to changes in signal-to-noise ratio down to $\langle \text{SNR} \rangle \sim 1$.

3. **Asymmetry must be defined at a given physical scale.** Both A_{CAS} and A_{RMS} show resolution dependence (Sec. 3.2.4 and 4.2), although it is more significant for A_{RMS} . However, this is not something that can be easily corrected: at higher resolutions, as we are able to resolve smaller structures, all galaxies become increasingly asymmetric (Sec. 6). Therefore, it is only meaningful to define asymmetry at a scale of features which constitute interesting ‘‘disturbances’’. We defined $A_{\text{RMS,x pc}}$, i.e. A_{RMS} measured at a given physical scale of x pc, and implemented a method to rescale and deconvolve images down to the chosen scale (Sec. 4.2). We tested its performance on observed data, where all images are rescaled to 200 parsec per pixel.

4. **$A_{\text{RMS,200 pc}}$ provides the best asymmetry measurements on observed data** (Sec. 5). When comparing measurements obtained for the same galaxies using *HST*, HSC, and SDSS imaging, only $A_{\text{RMS,200 pc}}$ results in unbiased measurements overall, while all other metrics underesti-

mate asymmetry in SDSS (due to a lower depth), HSC (due to a lower resolution), or both. While the $A_{\text{RMS,200 pc}}$ measurement has a relatively large scatter when using SDSS data, there is no bias between the error of galaxies that are intrinsically regular or disturbed. The scatter is likely due to observational effects such as artifacts, different source masks, deconvolution effects, and different Petrosian radii.

In Section 6, we discussed our findings and provided guidelines for best use cases given our results. Overall, A_{CAS} performs well in comparing data from deep surveys where $\langle \text{SNR} \rangle$ is high. However, when comparing results from heterogeneous surveys where resolution and/or depth may vary, $A_{\text{RMS,x pc}}$ is the most robust approach.

This is important for designing morphological studies and pipelines for future surveys, as well as comparing morphologies obtained in different studies. The source SNR varies during survey duration, from one observing run to another, and with cosmic time. A_{CAS} will result in inconsistent measurements in all of those cases. On the other hand, $A_{\text{RMS,x pc}}$ will provide robust measurements across different surveys, epochs, and studies, as well as enable us to use archival data with potentially extremely variable resolution and depth. Therefore, our suggested guideline for survey and pipeline development is:

1. Compute both A_{CAS} and A_{RMS} on native survey images;
2. Provide catalogs of $A_{\text{RMS,0.1''}}$ to allow easily comparison to other surveys;
3. Encourage scientists to evaluate $A_{\text{RMS,x pc}}$ for their samples of galaxies, especially if studying the redshift evolution of galaxy properties.

The algorithms used to compute A_{RMS} and $A_{\text{RMS,x pc}}$, including the deconvolution step, will be provided as an open source package as part of the larger Rubin morphology pipeline (Sazonova et al., in prep.).

ACKNOWLEDGEMENTS

We thank the University of Waterloo for their support of the Canada Rubin Fellowship program. ES thanks Roan Haggar and Ana Ennis for many fruitful scientific discussions throughout this project. R.D. gratefully acknowledges support by the ANID BASAL project FB210003. D.D. acknowledges support from the National Science Center (NCN) grant SONATA (UMO-2020/39/D/ST9/00720). MF has been supported by the Polish National Agency for Academic Exchange (Bekker grant BPN/BEK/2023/1/00036/DEC/01), and acknowledges support from the Polish National Science

Centre via the grant UMO-2022/47/D/ST9/00419. JR acknowledges funding from University of La Laguna through the Margarita Salas Program from the Spanish Ministry of Universities ref. UNI/551/2021-May 26, and under the EU Next Generation.

Facilities: HST (WFC3, ACS, WFPC2); 2.5m Sloan Digital Sky Survey (SDSS) Telescope at Apache Point Observatory (APO), National Astronomical Observatory of Japan (NAOJ) 8.2m Subaru Telescope at Mauna

Kea Observatory.

Software: GALSIM (Rowe et al. 2015), statmorph (Rodríguez-Gómez et al. 2019), photutils (Bradley et al. 2020), astropy (Astropy Collaboration et al. 2013, 2018; Collaboration et al. 2022b), Scikit-Image (van der Walt et al. 2014), Matplotlib (Hunter 2007), pandas (Reback et al. 2020), NumPy (Harris et al. 2020), SciPy (Virtanen et al. 2020)

REFERENCES

Abadi M. G., et al., 1999, *MNRAS*, 308, 947
 Abraham R. G., et al., 1996, *ApJS*, 107, 1
 Ackermann S., et al., 2018, *MNRAS*, 479, 415
 Aihara H., et al., 2022, *PASJ*, 74, 247
 Arnouts S., et al., 2007, *A&A*, 476, 137
 Astropy Collaboration et al., 2013, *A&A*, 558, A33
 Astropy Collaboration et al., 2018, *AJ*, 156, 123
 Baldry I. K., et al., 2004, *ApJ*, 600, 681
 Baldry I. K., et al., 2006, *MNRAS*, 373, 469
 Balogh M. L., et al., 2004, *ApJ*, 615, L101
 Bell E. F., et al., 2004, *The Astrophysical Journal*, 608, 752
 Benson A. J., et al., 2003, *ApJ*, 599, 38
 Bignone L. A., et al., 2017, *MNRAS*, 465, 1106
 Bignone L. A., et al., 2020, *MNRAS*, 491, 3624
 Blanton M. R., et al., 2017, *AJ*, 154, 28
 Bluck A. F. L., et al., 2023, *ApJ*, 944, 108
 Bottrell C., et al., 2019, *MNRAS*, 490, 5390
 Bottrell C., et al., 2024, *MNRAS*, 527, 6506
 Bradbury J., et al., 2018, JAX: composable transformations of Python+NumPy programs, <http://github.com/google/jax>
 Bradley L., et al., 2020, astropy/photutils: 1.0.1, doi:10.5281/zenodo.596036, <https://ui.adsabs.harvard.edu/abs/2020zenodo....596036B>
 Cantale N., et al., 2016, *A&A*, 589, A81
 Ceverino D., et al., 2014, *MNRAS*, 442, 1545
 Ciambur B. C., Graham A. W., 2016, *MNRAS*, 459, 1276
 Cicone C., et al., 2014, *A&A*, 562, A21
 Collaboration P., et al., 2020, *A&A*, 641, A6
 Collaboration E., et al., 2022a, *A&A*, 662, A112
 Collaboration A., et al., 2022b, *ApJ*, 935, 167
 Conselice C. J., 1997, *PASP*, 109, 1251
 Conselice C. J., 2003, *ApJS*, 147, 1
 Conselice C. J., et al., 2000, *ApJ*, 529, 886
 Conselice C. J., et al., 2008, *MNRAS*, 386, 909
 Deg N., et al., 2023, *MNRAS*, 523, 4340
 Desmons A., et al., 2023, *arXiv e-prints*, p. arXiv:2308.07962
 Domínguez Sánchez H., et al., 2018, *MNRAS*, 476, 3661
 Domínguez Sánchez H., et al., 2023, *MNRAS*, 521, 3861
 Ellison S. L., et al., 2008, *AJ*, 135, 1877
 Ellison S. L., et al., 2013, *MNRAS*, 435, 3627
 Faber S. M., et al., 2007, *ApJ*, 665, 265
 Ferrari F., et al., 2015, *ApJ*, 814, 55
 Ferreira L., et al., 2022, *ApJ*, 931, 34
 Gan F. K., et al., 2021, *arXiv e-prints*, p. arXiv:2103.09711
 Geda R., et al., 2022, *AJ*, 163, 202
 Giese N., et al., 2016, *MNRAS*, 461, 1656
 Graham A. W., Driver S. P., 2005, *PASA*, 22, 118
 Gunn J. E., Gott III J. R., 1972, *ApJ*, 176, 1
 Harris C. R., et al., 2020, *Nature*, 585, 357
 Heckman T. M., et al., 1990, *ApJS*, 74, 833
 Holwerda B. W., et al., 2011, *MNRAS*, 416, 2401
 Holwerda B. W., et al., 2012, *MNRAS*, 427, 3159
 Holwerda B. W., et al., 2023, *MNRAS*, 521, 1502
 Hopkins P. F., et al., 2009, *ApJ*, 691, 1424
 Hopkins P. F., et al., 2018, *MNRAS*, 480, 800
 Hunter J. D., 2007, *Computing in Science & Engineering*, 9, 90
 Ivezić Ž., et al., 2019, *ApJ*, 873, 111
 Jia P., et al., 2024, *MNRAS*, 527, 6581
 Kruk S. J., et al., 2018, *MNRAS*, 473, 4731
 LSST Dark Energy Science Collaboration et al., 2020, *The Astrophysical Journal Supplement Series*, 253, 31
 Leroy A. K., et al., 2015, *ApJ*, 814, 83
 Lintott C. J., et al., 2008, *MNRAS*, 389, 1179
 Lotz J. M., et al., 2004, *AJ*, 128, 163
 Lotz J. M., et al., 2011, *ApJ*, 742, 103
 Lucy L. B., 1974, *AJ*, 79, 745
 Mandelbrot B., 1967, *Science*, 156, 636
 Martig M., et al., 2009, *ApJ*, 707, 250
 Masters K. L., et al., 2010, *MNRAS*, 405, 783
 Masters K. L., et al., 2012, *MNRAS*, 424, 2180
 Michalewicz K., et al., 2023, *The Journal of Open Source Software*, 8, 5340
 Millon M., et al., 2024, *arXiv e-prints*, p. arXiv:2402.08725
 Nelder J. A., Mead R., 1965, *The Computer Journal*, 7, 308
 Nelson D., et al., 2019, *Computational Astrophysics and Cosmology*, 6, 2
 Nevin R., et al., 2019, *ApJ*, 872, 76
 Pawlik M. M., et al., 2016, *MNRAS*, 456, 3032
 Peng Y.-j., et al., 2010, *ApJ*, 721, 193
 Petrosian V., 1976, *ApJ*, 210, L53
 Pillepich A., et al., 2018, *MNRAS*, 473, 4077
 Piotrowska J. M., et al., 2022, *MNRAS*, 512, 1052
 Poggianti B. M., et al., 2017, *ApJ*, 844, 48
 Quinn P. J., 1984, *ApJ*, 279, 596
 Reback J., et al., 2020, pandas-dev/pandas: Pandas 1.1.3, doi:10.5281/ZENODO.4067057
 Richardson W. H., 1972, *Journal of the Optical Society of America* (1917-1983), 62, 55
 Rodríguez-Gómez V., et al., 2019, *MNRAS*, 483, 4140
 Román J., et al., 2020, *A&A*, 644, A42
 Rowe B. T. P., et al., 2015, *Astronomy and Computing*, 10, 121
 Sazonova E., et al., 2021, *ApJ*, 919, 134
 Schade D., et al., 1995, *ApJ*, 451, L1
 Schwanski K., et al., 2014, *MNRAS*, 440, 889
 Schweizer F., 1980, *ApJ*, 237, 303
 Sérsic J. L., 1963, *Boletín de la Asociación Argentina de Astronomía La Plata Argentina*, 6, 41
 Shi Y., et al., 2009, *ApJ*, 697, 1764
 Shibuya T., et al., 2022, *PASJ*, 74, 73
 Snyder G. F., et al., 2015, *MNRAS*, 451, 4290
 Snyder G. F., et al., 2019, *MNRAS*, 486, 3702
 Strateva I., et al., 2001, *AJ*, 122, 1861
 Taylor E. N., et al., 2015, *MNRAS*, 446, 2144
 Thompson R., et al., 2015, *arXiv e-prints*, p. arXiv:1508.01851
 Thorp M. D., et al., 2021, *MNRAS*, 507, 886
 Tohill C., et al., 2021, *ApJ*, 916, 4
 Toomre A., Toomre J., 1972, *ApJ*, 178, 623
 Vega-Ferrero J., et al., 2024, *ApJ*, 961, 51
 Virtanen P., et al., 2020, *Nature Methods*, 17, 261
 Walmsley M., et al., 2022, *MNRAS*, 509, 3966
 Wen Z. Z., Zheng X. Z., 2016, *ApJ*, 832, 90
 Werner N., et al., 2019, *Space Sci. Rev.*, 215, 5
 Wiener N., 1949, *Extrapolation, Interpolation, and Smoothing of Stationary Time Series: With Engineering Applications*. The MIT Press, doi:10.7551/mitpress/2946.001.0001
 Wilkinson S., et al., 2024, *MNRAS*
 Willett K. W., et al., 2013, *MNRAS*, 435, 2835
 Yagi M., et al., 2006, *MNRAS*, 368, 211
 York D. G., et al., 2000, *AJ*, 120, 1579
 Yu S.-Y., et al., 2023, *A&A*, 676, A74
 van der Walt S., et al., 2014, *PeerJ*, 2, e453

APPENDIX

A. MINIMIZATION

As defined in Eq. 1 and Eq. 4, both asymmetry metrics require finding a center of rotation \mathbf{x}_0 such that asym-

metry is minimized.

Initially, asymmetry center was found through a grid search around the brightest pixel (e.g., Conselice et al. 2000); however, doing so for a sufficiently large search radius is computationally expensive. In modern applications, a numerical algorithm (such as Nelder-Mead; Nelder & Mead 1965) is used to find a minimum of the asymmetry function. In this function, the image is first rotated using Scikit-Image `rotate` or equivalent, and then asymmetry is calculated. By default, \mathbf{x}_0 is allowed to vary continuously during minimization, meaning that rotation is performed about a fractional pixel. This requires interpolation, which adds correlations between background pixels in the rotated image that are not present in the original image. Because of these added correlations, the sky background of the original and the rotated images are no longer the same, and so calculating or even defining a background asymmetry term becomes challenging.

One solution is to not allow rotations about fractional pixel values (or at most, allow half-pixel centers, as done in Yagi et al. 2006). However, minimization algorithms are not well-defined when the possible domain is discrete. Instead, we allowed rotation centers to vary continuously, but set the `rotate` function to perform 0th-order interpolation, therefore avoiding any artifacts.

Another important step in the minimization is deciding on the initial guess for \mathbf{x}_0 . Since most algorithms perform a gradient-based search for a local minimum, starting with a poor guess for the global \mathbf{x}_0 can lead the minimizer towards a local minimum. A typical choice (e.g., in `statmorph`) is to use the first moment of the light distribution, or a flux-weighted center. This choice is actually a local *maximum* of the asymmetry residual for most light distributions, and so a gradient-based minimizer may often converge on the wrong minimum.

Another concern is that minimization is the most computationally intensive step of the calculation, as it requires re-computing asymmetry for different \mathbf{x}_0 guesses. While traditionally optimization algorithms such as Nelder-Mead (Nelder & Mead 1965) are used, a significant boost in performance can be obtained by using gradient-based algorithms, or using tools that leverage automatic differentiation (such as Jax; Bradbury et al. 2018).

Finally, it may be possible to find the optimal center of the A_{RMS} asymmetry without a computationally expensive minimization routine. While this is beyond the scope of this paper, we provide a quick proof-of-concept of this possibility.

Consider a noiseless, PSF-free, *true* RMS asymmetry as defined in Eq. 4:

$$A_{\text{RMS}}^2 = \min_{\mathbf{x}_0} \frac{\int_{-\infty}^{\infty} (\mathcal{I} - \mathcal{I}^{180})^2 d\mathbf{x}}{\int_{-\infty}^{\infty} \mathcal{I}^2 d\mathbf{x}}. \quad (\text{A1})$$

The integral in the denominator is simply a normalization term, and since it is independent of \mathbf{x}_0 , it can be omitted from optimization; so we only need to optimize the residual,

$$R = \min_{\mathbf{x}_0} \int_{-\infty}^{\infty} (\mathcal{I} - \mathcal{I}^{180})^2 d\mathbf{x}. \quad (\text{A2})$$

For this proof-of-concept exercise, we ignore that asymmetry is calculated within an aperture – this does not affect the results in the noiseless case. Finally, for simplicity, we only consider this equation in one dimension; however, the calculations extend easily to multiple dimensions.

We can define a rotation by 180° as $\mathcal{I}^{180} = \mathcal{I}(x - 2x_0)$ for some rotation center x_0 . Then we need to find \mathbf{x}_0 such that

$$\frac{\partial R}{\partial x_0} = \frac{\partial}{\partial x_0} \int_{-\infty}^{\infty} (\mathcal{I}(x) - \mathcal{I}(x - 2x_0))^2 dx = 0. \quad (\text{A3})$$

Taking the partial derivative and expanding the square, we get:

$$0 = \int_{-\infty}^{\infty} \mathcal{I}'(x - 2x_0) [\mathcal{I}(x) - \mathcal{I}(x - 2x_0)] dx \quad (\text{A4})$$

$$= \int_{-\infty}^{\infty} \mathcal{I}'(x - 2x_0) \mathcal{I}(x) dx - \int_{-\infty}^{\infty} \mathcal{I}'(u) \mathcal{I}(u) du \quad (\text{A5})$$

$$= \mathcal{I} \star \mathcal{I}'(-2x_0) - \frac{1}{2} \mathcal{I}^2(u) \Big|_{-\infty}^{\infty}. \quad (\text{A6})$$

Since the galaxies' flux vanishes at infinity, the second term is zero, therefore we need to find the zeros of the cross-correlation function between \mathcal{I} and \mathcal{I}' . We can use the Fourier cross-correlation theorem:

$$0 = \mathcal{I} \star \mathcal{I}'(-2x_0) = \mathcal{F} \left[\mathcal{I} \star \mathcal{I}'(2x_0) \right] \quad (\text{A7})$$

$$= \frac{1}{2} \bar{\mathcal{I}} \left(\frac{\xi}{2} \right) \hat{\mathcal{I}}' \left(\frac{\xi}{2} \right) = \frac{1}{2} \bar{\mathcal{I}} \times \pi i \xi \hat{\mathcal{I}} \left(\frac{\xi}{2} \right) \quad (\text{A8})$$

$$= i \pi \xi \left| \hat{\mathcal{I}} \left(\frac{\xi}{2} \right) \right|^2. \quad (\text{A9})$$

Therefore, finding the theoretical asymmetry minimum of a noiseless distribution requires simply calculating the power spectrum of the image, and then finding a zero of this power spectrum – although one would still need to find the zero that corresponds to the global minimum. While root-finding is still required, this is a much simpler problem to solve computationally than rotating the image and finding the asymmetry value at each rotation center. However, noise, discretization, and the PSF will

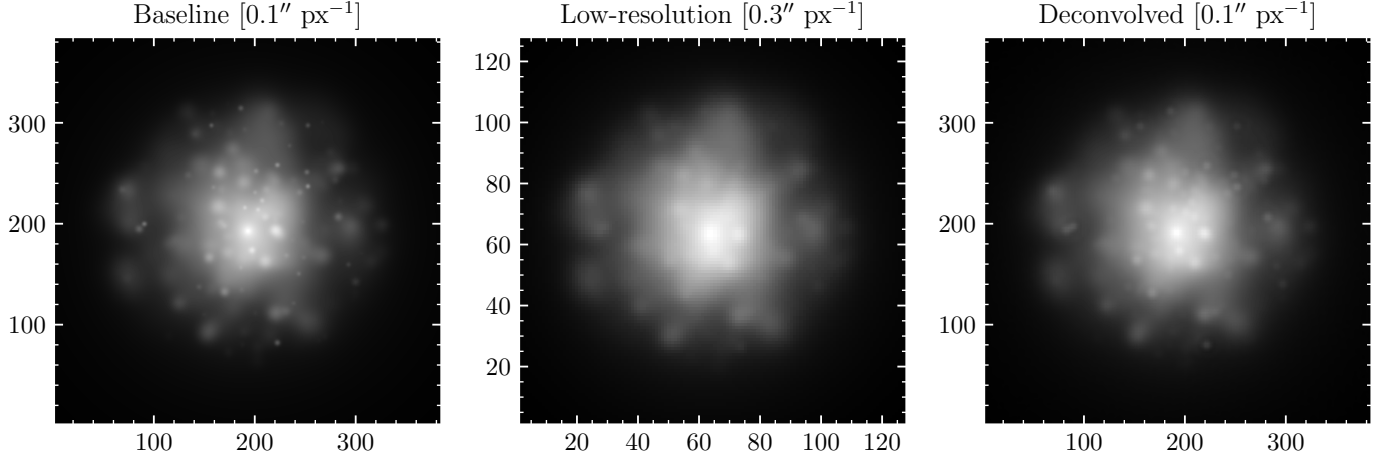


FIG. A1.— An example galaxy under deconvolution. **Left:** the baseline image generated on a $0.1''$ pixel scale with a $0.3''$ Gaussian PSF. **Middle:** a “mock” observation generated on a $0.3''$ pixel scale, with a $0.9''$ Gaussian PSF, sky surface brightness of 30 mag/arcsec^2 , and Poisson noise. **Right:** the mock image, after being resampled onto a $0.1'' \text{ px}^{-1}$ grid and deconvolved. Most small-scale features are recovered, although the smallest scales are lost as they cannot be recovered during interpolation.

affect this calculation. Determining whether an analytic \mathbf{x}_0 in a realistic observation exists is beyond the scope of this paper, but is an interesting avenue to explore.

B. BACKGROUND ESTIMATION

Correctly estimating and subtracting the background contribution to asymmetry is crucial. This is a non-trivial task, since in theory, we need to estimate the contribution of the background that the source is overlayed on top of – which is impossible without subtracting the source. In practice, many implementations will calculate the sky asymmetry in a blank patch of the sky, and extrapolate this to the expected asymmetry in the source aperture.

Different algorithms take slightly different approaches. For example, `statmorph` finds the largest possible *blank* sky patch (i.e., a patch with no other sources found during the segmentation routine), and simply transpose the background to get the rotated sky. While this approach would give the correct background estimate for a purely Gaussian white noise sky, it will not be able to correct for possible large-scale fluctuations in the background.

Another approach is to calculate the background in *several* sky patches randomly placed in the image away from the source (e.g., in MORFOMETRYKA; Ferrari et al. 2015). While similar to the `statmorph` algorithm, this approach is more robust against random fluctuations that may affect the background measurement in a single patch. Moreover, it is possible to then reconstruct the overall sky gradients and find large-scale asymmetries.

In our tests, we opted to compute the sky background in annuli centered on the asymmetry center, similarly to the source asymmetry. This is the same approach as that used in typical photometry applications. There are several advantages to this method. First, we are able to capture any large-scale sky fluctuations. Second, the

sky is rotated the same way as the image about the same center, therefore we are correctly estimating the sky contribution *under the same rotation*. Finally, although we mask any extraneous sources both in the source and the sky aperture, any faint non-Gaussian sources (e.g., undetected stars or galaxies), will be included in our sky asymmetry estimate.

C. DECONVOLUTION

While in ideal noiseless observations deconvolution is a simple procedure, the addition of noise makes deconvolution an ill-posed problem, as noise terms are amplified by the inverse of the PSF. Iterative procedures, such as Richardson-Lucy deconvolution (Richardson 1972; Lucy 1974) or newer methods (e.g., Michalewicz et al. 2023) produce better results, but as they depend on numerical minimization, are computationally expensive. Instead, we turn to a simpler approach, motivated by the Wiener filter: deconvolving the image in Fourier space by penalizing noise-dominated high-frequency terms.

An observed distribution $I = \lambda * \mathcal{I} + \epsilon$ can be expressed in Fourier space as $\hat{I} = \hat{\lambda} \hat{\mathcal{I}} + \hat{\epsilon}$, where $\hat{\cdot}$ represents a Fourier transform. In theory, dividing by the PSF in Fourier space should recover the original distribution, \mathcal{I} . However, since $\hat{\lambda}^{-1} \rightarrow 0$ at high frequencies and Gaussian noise is constant at all frequencies, high-frequency noise terms are amplified.

The Wiener transform, H_W (Wiener 1949), aims to dampen the noise-dominated high-frequency terms while preserving the frequencies with high SNR. It is derived by minimizing the expected error between the deconvolved and the true images, $\langle |\hat{H}_W \hat{I} - \hat{\mathcal{I}}|^2 \rangle$. A Wiener transform acts essentially as a low-pass filter, setting high-frequency terms to 0. While this recovers the low-frequency features in the image, it can also add visible artifacts, since all high-frequency terms are removed. With these goals

in mind, we want to find a transform H that minimizes the error

Following the Wiener approach, we derive a new transform. The modifications of our method are two-fold: 1) first, we aim to recover the original noise level rather than denoise the image; and second, we do not fully deconvolve the image following the example in [Cantale et al. \(2016\)](#) – instead, we deconvolve it down to the Nyquist frequency. Both of these modifications help us remove denoising and Gibbs ringing artifacts.

Therefore, we want to recover a Nyquist-sampled and noisy image, accounting only for the smearing by the PSF: $\lambda_{3px} * \mathcal{I} + \epsilon$, where λ_{3px} is a Gaussian PSF with a 3-pixel FWHM. We opted for retaining the noise term, since this reduces the artefacts introduced by denoising, and we have already shown that A_{RMS} is independent of the SNR of the image. Therefore, we need to find a transform H such that

$$HI(x, y) = \lambda_{3px} * \mathcal{I} + \epsilon \quad (\text{C1})$$

We can find H by minimizing the expected difference between the right-hand and the left-hand sides of this equation, or

$$\min_H \mathbb{E} |\hat{H}\hat{I} - (\hat{\lambda}_{3px}\hat{\mathcal{I}} + \hat{\epsilon})|^2 \quad (\text{C2})$$

Taking a partial derivative with respect to \hat{H} , we find that the optimal filter must take the form

$$\hat{H}^* = \frac{\hat{\lambda}\hat{\lambda}_{3px}^* + |\widehat{\text{SNR}}|^{-2}}{|\hat{\lambda}|^2 + |\widehat{\text{SNR}}|^{-2}} \quad (\text{C3})$$

where $\widehat{\text{SNR}}$ is the signal-to-noise ratio term which damps the effect of the transform at noise-dominated frequencies.

For a perfect deconvolution, $\widehat{\text{SNR}}$ must be equal to $\langle |\mathcal{I}|^2 \rangle / \langle |\epsilon|^2 \rangle$. However, this requires knowledge of the original distribution \mathcal{I} and so is impossible to calculate directly. In photography, often one can assume that SNR decays with spatial frequency ω as $\text{SNR} \propto \omega^{-2}$. However, in general this is not true, and a careful estimate of $\widehat{\text{SNR}}$ is required for this deconvolution approach to work well.

Instead of relying on any assumptions, we approximate $\widehat{\text{SNR}}$ from the observed images. We get the first order estimate by calculating it directly from the noisy image:

D. OBSERVED SAMPLE

Here we provide the properties of the galaxies, instruments, and images used in the observational test in Sec. 5, as well as the measured asymmetry values for each galaxy. Refer to Table D below.

This paper was built using the Open Journal of Astrophysics L^AT_EX template. The OJA is a journal which provides fast and easy peer review for new papers in the `astro-ph` section of the arXiv, making the reviewing process simpler for authors and referees alike. Learn more at <http://astro.theoj.org>.

$\widehat{\text{SNR}}' = \hat{I}/\hat{\epsilon}$. This calculation has two issues. First, as noise dominates the signal at high frequencies, $\hat{I}/\hat{\epsilon} \rightarrow 1$ while the true $\widehat{\text{SNR}} \rightarrow 0$. Therefore, we need some estimate of SNR in noise-dominated pixels.

First, we mask all pixels with $\widehat{\text{SNR}}$ below a threshold (80th percentile or 3, whichever is higher), since we cannot use pixels where the noise contributes significantly to the “signal” measurement. Then, we find the 0th frequency $\widehat{\text{SNR}}$, corresponding to the total SNR of the galaxy. We set the highest frequency $\widehat{\text{SNR}}$ to 10^4 lower. We chose this value as it means that the light distribution spans roughly 10 magnitudes, consistent with the expected brightness difference between integrated light and the faint outer features. This produces a $\widehat{\text{SNR}}$ array where only the lowest- and the highest-frequency terms are populated: we then interpolate between these to fill the remaining values.

Second, while the interpolation mitigates the overestimation of $\widehat{\text{SNR}}$ at high frequencies, the resulting $\widehat{\text{SNR}}'$ effectively recovers $\hat{\lambda}\hat{I}/\hat{\epsilon}$ and thus underestimates the true $\widehat{\text{SNR}}$. Therefore, we further correct our $\widehat{\text{SNR}}'$ for the effect of the convolution by the PSF, estimating the intrinsic $\widehat{\text{SNR}}$ as:

$$\widehat{\text{SNR}} = \frac{\widehat{\text{SNR}}'}{\hat{\lambda} + \widehat{\text{SNR}}'} \quad (\text{C4})$$

Fig. A1c) shows the image deconvolved with our H . Unlike the Wiener deconvolution, our approach retains the original noise, thereby reducing the amount of artefacts that may affect the asymmetry measurement. We note that since the highest-frequency terms (e.g., point sources) are lost to the noise, it is impossible to recover them using our approach to deconvolution, and machine learning-based techniques are necessary to recover terms that are completely unresolved. Moreover, if computational time is not a constraint, more accurate optimization-based deconvolution methods may be used (e.g., [Millon et al. 2024](#)). However, our algorithms achieves reasonable performance in a fraction of the time required by optimization methods – since the only bottleneck of this method is performing a fast Fourier transform, which takes less than a second for all but the largest image cutouts.

TABLE D1
PROPERTIES OF THE OBSERVED DATASET

Type	Galaxy properties			HST						HSC						SDSS					
	log M/M _⊙	<i>z</i>	200 pc [<i>V</i>]	Depth	ACAS	A _{corr}	ARMS	A _{RM^{200pc}}	Depth	ACAS	A _{corr}	ARMS	A _{RM^{200pc}}	Depth	ACAS	A _{corr}	ARMS	A _{RM^{200pc}}			
PSB	10.8	0.139	0.079	23.7	0.18	0.23	0.70	0.62	26.2	0.36	0.36	0.56	0.62	23.7	0.09	0.11	0.49	0.59			
PSB	10.2	0.048	0.206	23.7	0.06	0.07	0.45	0.25	25.2	0.06	0.06	0.29	0.34	23.6	0.05	0.05	0.41	0.30			
SFG	10.2	0.047	0.209	26.1	0.18	0.18	0.46	0.36	25.2	0.11	0.11	0.35	0.37	23.8	0.09	0.09	0.40	0.36			
PSB	11.0	0.129	0.084	23.7	0.17	0.19	0.52	0.44	26.4	0.13	0.13	0.37	0.43	23.8	0.05	0.05	0.36	0.44			
PSB	10.2	0.033	0.294	23.7	0.10	0.39	0.34	0.26	0.10	0.10	0.37	0.30	23.8	0.15	0.15	0.46	0.48				
QG	10.4	0.092	0.113	25.8	0.04	0.04	0.25	0.31	27.9	0.06	0.06	0.30	0.24	23.6	0.05	0.06	0.37	0.36			
SFG	10.6	0.125	0.086	25.8	0.30	0.30	0.53	0.50	28.0	0.27	0.27	0.47	0.51	23.6	0.14	0.15	0.52	0.48			
SFG	10.6	0.119	0.090	25.8	0.08	0.08	0.34	0.34	28.0	0.09	0.09	0.32	0.37	23.6	0.07	0.08	0.37	0.37			
QG	10.9	0.125	0.086	25.7	0.14	0.14	0.50	0.41	27.9	0.13	0.13	0.24	0.34	23.8	0.06	0.07	0.35	0.15			
SFG	11.0	0.133	0.082	25.8	0.05	0.05	0.23	0.39	28.0	0.11	0.11	0.33	0.37	23.7	0.06	0.07	0.45	0.28			
SFG	10.9	0.165	0.068	25.8	0.11	0.11	0.34	0.28	28.1	0.09	0.09	0.28	0.30	23.7	0.02	0.03	0.39	0.39			
QG	10.3	0.080	0.128	25.8	0.09	0.09	0.29	0.38	28.1	0.06	0.06	0.46	0.35	23.8	0.08	0.08	0.36	0.23			
QG	10.7	0.104	0.102	25.8	0.15	0.15	0.48	0.39	28.1	0.08	0.08	0.36	0.44	23.8	0.10	0.11	0.44	0.31			
QG	10.8	0.092	0.113	25.8	0.12	0.12	0.48	0.37	28.1	0.07	0.07	0.28	0.35	23.6	0.04	0.04	0.35	0.24			
SFG	10.2	0.107	0.099	25.8	0.14	0.15	0.47	0.41	28.1	0.16	0.16	0.38	0.44	23.6	0.01	0.01	0.37	0.46			
SFG	10.5	0.076	0.135	25.8	0.16	0.61	0.46	0.28	0.17	0.17	0.43	0.52	23.7	0.10	0.11	0.45	0.46				
SFG	10.8	0.092	0.113	25.8	0.23	0.24	0.49	0.49	27.8	0.22	0.22	0.44	0.48	24.1	0.08	0.09	0.42	0.45			
QG	11.0	0.123	0.087	25.7	0.02	0.02	0.20	0.27	26.9	0.04	0.04	0.30	0.23	23.7	0.04	0.04	0.30	0.23			
QG	11.2	0.175	0.065	25.9	0.05	0.05	0.31	0.37	27.8	0.08	0.08	0.31	0.28	23.8	0.02	0.02	0.28	0.28			
SFG	10.2	0.063	0.161	25.3	0.15	0.16	0.49	0.41	27.7	0.21	0.21	0.40	0.44	23.7	0.07	0.08	0.47	0.52			
QG	10.9	0.087	0.119	25.1	0.05	0.05	0.40	0.35	25.6	0.03	0.03	0.29	0.25	23.6	0.05	0.05	0.39	0.31			
SFG	10.8	0.082	0.126	25.9	0.08	0.08	0.29	0.35	26.3	0.07	0.07	0.31	0.41	23.8	0.09	0.09	0.44	0.27			
QG	10.5	0.082	0.126	25.9	0.08	0.08	0.27	0.25	26.2	0.08	0.08	0.24	0.43	23.9	0.11	0.11	0.42	0.29			
SFG	10.2	0.028	0.340	25.1	0.17	0.18	0.84	0.45	25.7	0.20	0.20	0.44	0.39	23.9	0.12	0.13	0.46	0.47			
QG	10.4	0.066	0.153	25.2	0.08	0.09	0.53	0.51	26.8	0.16	0.16	0.48	0.54	23.9	0.07	0.09	0.48	0.48			
SFG	10.7	0.175	0.065	25.8	0.14	0.15	0.48	0.38	25.9	0.12	0.12	0.47	0.40	23.9	0.12	0.01	0.40	0.44			
SFG	10.9	0.188	0.062	25.9	0.18	0.19	0.51	0.49	25.9	0.18	0.18	0.46	0.50	23.8	0.09	0.12	0.51	0.59			